High-T$_c$ SQUIDs: Noise and Applications

A Dissertation Presented to

the Faculty of the Department of Physics

University of Houston

In Partial Fulfillment

of the Requirements for the Degree of

Doctor of Philosophy

By

Hsiao-Mei Cho

August 2001

High-Tc SQUIDs: Noise and Applications

_____

Hsiao-Mei Cho

APPROVED:

_____

Dr. Paul C. W. Chu, Chirman

_____

Dr. John Clarke, Co-Chairman

Physics dept. UC-Berkeley

_____

Dr. John C. Wolfe

Department of Electrical and

Computer Engineering

_____

Dr. Alex Ignatiev

_____

Dr. Chin-Sen Ting

Acknowledgement

In Chinese one way to express one's gratitude toward many people is to say "Thank God!" Indeed, I thank God to bring me together with many nice people who helped me to achieve my degree. It would not have been possible to complete my degree without any one of them.

My foremost thanks go to my advisors, Prof. Paul C. W. Chu and Prof. John Clarke. Prof. Chu has been my benefactor. When I needed support to continue doing the research projects that I was interested in, he gave me the support and freedom to do whatever I would love to do. Throughout these years, his generosity and kindness made my dreams come true. Meanwhile, Prof. John Clarke has been my mentor. He provided me a stimulating and exciting research environment and topics that were both interesting and important. His vast knowledge always helped me through many challenges and difficulties in my work. His kindness allowed me to break a couple of bicrystals. His attitude on research required me to learn everything from the very basis and to build up my knowledge from a very good foundation.

My special thanks go to Dr. Saburo Tanaka, Dr. Gene Dantsker, Dr. Byungdu Oh, Dr. Konstantin Kouznetsov, Dr. Yann Chelma and Robert McDermott for teaching me the delicate art of high-T_c devices, from fabricating thin films to measuring the noise of the devices. Their patience and knowledge have been transferred to me.

University of Houston and the Texas Center for Superconductivity at UH. They took care of the administrative paperwork for me so that I could concentrate on my research.

Besides those who helped me directly in my research, I would also like to express appreciation to my host family, Sonia Long and my friends: Dr. Chonglin Chen, Dr. James Claycomb, Wesley Hsieh, Maggie Hsu, Louisa Lee, Grace Lin, Eliza Tsai, Kuei-Ling Tsui, Hsiao-Wen Yu and all other friends whose names I cannot spell in English. Their encouragement and help gave me strength to finish my degree.

Finally, I would like to thank my family, especially my sisters, Hsiao-Hua and Hisao-Ching. I am grateful for their support and understanding. All these years, they gave me freedom to do what I want to do with their full support. When I had doubts about myself, their confidence in me made me strong and special. When I was homesick, they bought me tickets to go home. I also want to dedicate this thesis to the loving memory of my grandparents.

High-T$_c$ SQUIDs: Noise and Applications

An Abstract of a Dissertation

Presented to

the Faulty of the Department of Physics

University of Houston

In Partial Fulfillment

of the Requirements for the Degree of

Doctor of Philosophy

By

Hsiao-Mei Cho

August 2001

Abstract

A major challenge in the design and operation of high transition temperature (T_c) Superconducting Quantum Interference Devices (SQUIDs) is their potential to exhibit substantially higher levels of noise at low frequency f when exposed to earth's magnetic field. To investigate this problem, we studied the noise of high-T_c SQUIDs, directly coupled magnetometers and multilayer magnetometers in both static and changing magnetic fields. The directly coupled magnetometer consists of a dc SQUID connected to a large area pickup loop in parallel. The multilayer magnetometer involves a multiturn flux transformer inductively coupled to a dc SQUID on a separate substrate. All the devices are made of thin films of the high-T_c superconductor $YBa_2Cu_3O_{7-\delta}$, patterned into 4 μm linewidths.

After cooling in a magnetic field, the devices showed no increase in 1/f noise for fields up to threshold values well above the earth's magnetic field. The devices were also cooled in a magnetic field that was subsequently turned off. The 1/f noise of bare SQUIDs was unchanged for fields up to 12 μT. The addition of the flux transformer containing flux dams increased the sensitivity to magnetic field by a factor of 43 while reducing the threshold field only moderately, to 5 μT. This result implies that the multilayer magnetometer can be rotated in the earth's magnetic field through an angle of up to 26° without increasing the low frequency noise.

The results of these studies were incorporated into a 5-channel high-T_c magnetocardiography system involving two first-derivative SQUID gradiometers and three reference SQUIDs. Each planar gradiometer consists of a directly coupled SQUID magnetometer inductively coupled to the smaller coil of an asymmetric, two-loop flux transformer. The reference SQUIDs are patterned into 4 μm lines. The outputs of the five channels were subtracted in software to form a second-derivative gradiometer. Its long baseline, 48 mm, and good intrinsic balance, better than 1 part in 100, make the gradiometer an excellent candidate for measuring heart signals in an unshielded environment. Using this system, we obtained adult magnetocardiograms in ambient environments of sufficient quality for clinical applications.

Contents

List of Figures

Chapter I

Introduction

In 1962 Josephson[1] predicted a remarkable tunneling effect of Cooper pairs. Within a few years, many devices based on Josephson junctions were fabricated, most notably the Superconducting Quantum Interference Device (SQUID)[2,3], which is the most sensitive detector of magnetic flux. As a result, SQUIDs have been attractive devices for a variety of applications where one measures a tiny magnetic flux or magnetic field. In 1986, scientists were amazed and excited by the discovery of superconductivity in LaBaCuO by Bednorz and Muller[4], followed by superconductivity in $YBa_2Cu_3O_{7-\delta}$[5] (YBCO) with a transition temperature (T_c) of 92K, above the boiling point of liquid nitrogen, 77K. The discovery of high T_c superconductors has opened the way to develop SQUIDs and flux transformers operated in liquid nitrogen at 77K.

In this chapter, I begin with a brief review of the principles of Josephson junctions and dc SQUIDs followed by descriptions of high temperature superconducting (HTS) dc SQUIDs.

1.1   Josephson Junctions and Resistively Shunted Junction Model

A Josephson junction consists of two superconductors separated by a weak link, an insulating barrier, a normal metal layer or a grain boundary. In 1962 Brian Josephson[1]

predicted that Cooper pairs of electrons are able to tunnel through the weak link, maintaining phase coherence in the process. The applied current flowing between the two superconductors follows the current-phase relation

$$I = I_c \sin\phi, \tag{1.1}$$

where I_c is the critical current of the Josephson junction and ϕ is the phase difference between the two superconductors. When the current is less than the critical current I_c, the voltage across the junction is zero. On the other hand, when the current is larger than the critical current, a voltage appears according to the voltage-frequency relation

$$V = \frac{\hbar}{2e}\partial\phi/\partial t = \frac{\Phi_0}{2\pi}\partial\phi/\partial t \tag{1.2}$$

where the flux quantum $\Phi_0 = h/2e \approx 2 \times 10^{-15}$ T·m^2.

An equivalent circuit model to describe the Josephson junction is the resistively shunted junction (RSJ) model[6,7], shown in Fig. 1-1.The junction has a critical current I_c and is in parallel with its self-capacitance C and shunt resistance R. The equation of motion is

$$C\dot{V} + I_c \sin\phi + V/R = I. \tag{1.3}$$

If we replace $\dot{V}$ with Eq. (1.2), we obtain

$$I - I_c \sin\phi = \frac{\hbar C}{2e}\ddot{\phi} + \frac{\hbar}{2eR}\dot{\phi} = -\frac{2e}{\hbar}\frac{\partial U}{\partial\phi}, \tag{1.4}$$

where

$$U = -\frac{\Phi_0 I}{2\pi}\phi - \frac{\Phi_0 I_c}{2\pi}\cos\phi. \tag{1.5}$$
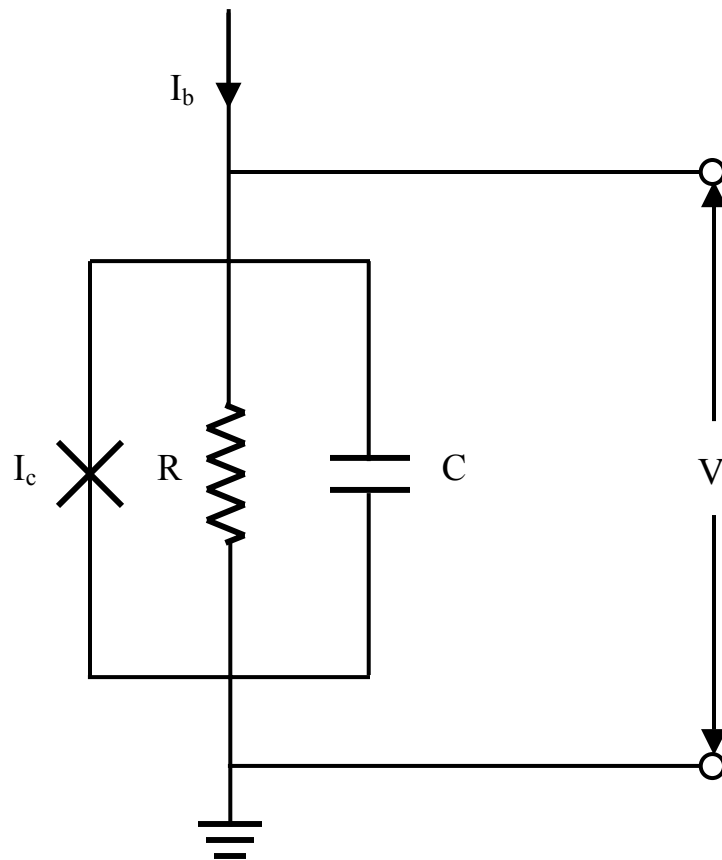
Fig. 1-1 The resistively shunted Josephson junction.

For zero applied current, the two superconductors are coupled by an energy $\Phi_0 I_c / 2\pi$.

Computer simulations by Clarke and Koch[8] have shown that a minimum value of critical current is required to remain the coupling between two sides of the junction. The condition is written as $I_c \Phi_0 / 2\pi \geq 5k_B T$. For a dc SQUID at 77K, as an example, the critical current $I_c \geq 16\mu A$. Since the self-capacitance of the HTS junction is small, we can rewrite Eq. (1 4) as $I = I_c \sin\phi + V/R$. The current-voltage relation can be obtained from the time average of V at constant current I:

$$<V> = RI_c <I/I_c - \sin\phi>. \qquad (1.6)$$

Therefore, one finds that the voltage across the junction is zero for $I \leq I_c$; for $I > I_c$, $V = I_c R [(I/I_c)^2 - 1]^{1/2}$.

1.2   dc SQUIDs

A dc SQUID consists of two Josephson junctions in parallel on a superconducting loop of inductance L[9]. The equivalent circuit diagram of the dc SQUID is shown in Fig. 1-2(a). We assume that both junctions are identical and arranged symmetrically on the loop. If an external flux is applied to the superconducting loop, the critical current of the junctions oscillates as a function of Φ with a period of Φ_0. As shown in Fig. 1-2(b) the maximum critical current occurs for $\Phi = n\Phi_0$; the minimum critical current appears for $\Phi = (n+1/2)\Phi_0$. Therefore, when the SQUID is biased with a current $I_b > I_c^{max}$, the voltage across the loop is modulated by the applied flux with a period of Φ_0 and amplitude ΔV, as shown in Fig. 1-2(c); this response is called the voltage-flux transfer function. In other

4

(a)

I

Φ

V

(b)

I

Φ = nΦ₀

Iᵦ

Φ = (n+1/2)Φ₀

V

(c)

V

0   1   2   Φ/Φ₀
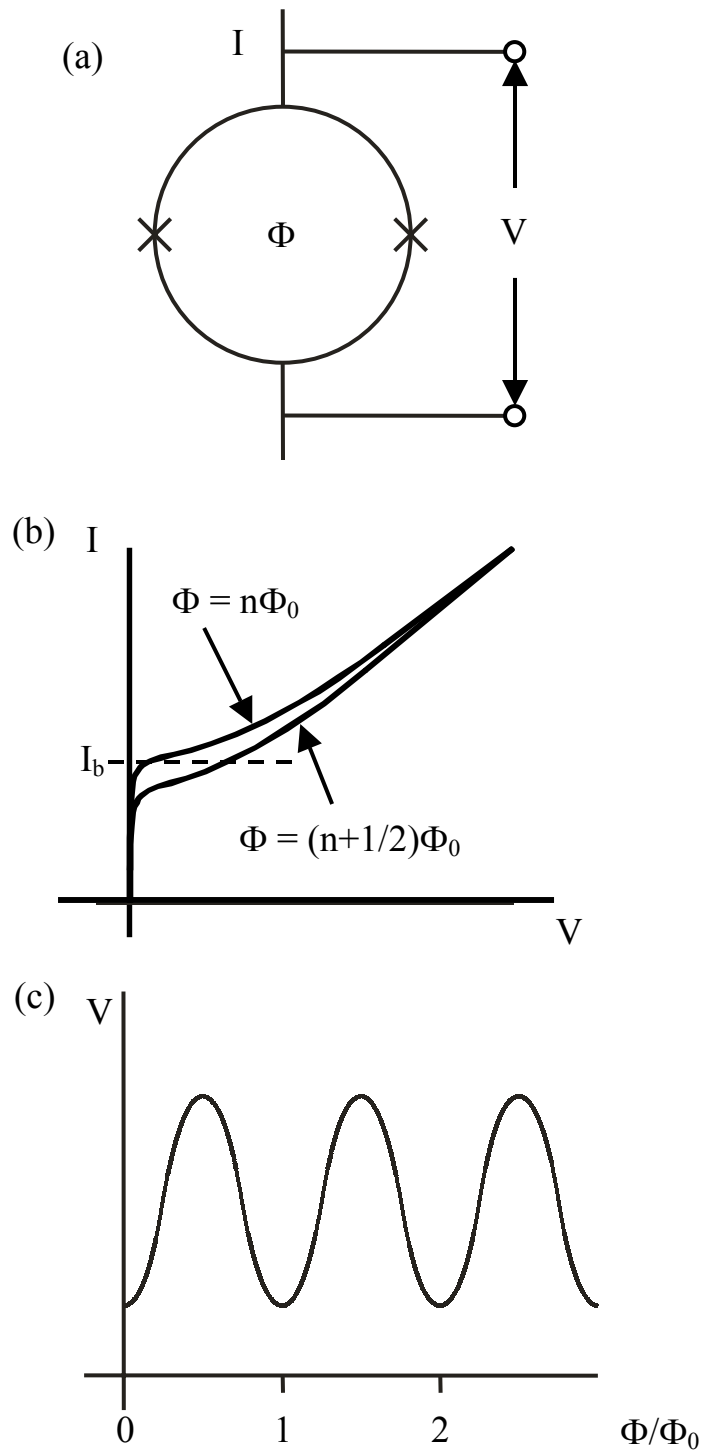
Fig. 1-2 (a) The dc SQUID; (b) I-V Characteristics; (c) V-Φ at constant bias current I_b.

5

words, the SQUID is a flux-to-voltage transducer with a maximum transfer function $V_\Phi = \partial V/\partial \Phi$ given by the V-Φ characteristic at the steepest point. Normally, one biases the SQUID at the current where V_Φ is a maximum. Thus the SQUID produces a maximum output signal $\delta V = V_\Phi \, \delta \Phi$ in response to a small flux signal $\delta \Phi$.

1.3   Noise in the dc SQUID

There are two main sources of noise in SQUIDs: thermal noise or white noise, and 1/f noise. The thermal noise in the SQUID results from Nyquist noise[10,11] currents in the junction resistors, which is frequency independent. Computer simulation[12,13] shows that a minimum noise energy is obtained for a reduced inductance $\beta_L = 2LI_c/\Phi_0 \approx 1$. At 4.2K and under optimum condition, $V_\Phi = R/L$ and the power spectral density of the voltage noise of the SQUID at 4.2K is $S_V(f) \approx 16 \, k_B TR$. Thus, the spectral density of the flux noise in the SQUID loop is given by $S_\Phi(f) = S_V(f)/V_\Phi^2 \approx 16 k_B TL^2/R$. It is sometimes convenient to introduce the concept of noise energy, $\varepsilon(f) = S_\Phi(f)/2L \approx 8 \, k_B TL/R$. Although these results cannot be immediately applied to SQUIDs at 77K, the qualitative result that lower temperatures and higher transfer functions reduce the SQUID flux noise is valid for both low-T_c and high-T_c SQUIDs.

Typical white noise of high-T_c SQUIDs is 10-20 $\mu\Phi_0/Hz^{1/2}$. To obtain a reasonable prediction of flux noise, the transfer function of the high-T_c SQUID needs to

be carefully calculated. Enpuku *et al.*[14] obtained an analytical expression for the transfer function of high-T_c SQUIDs,

$$V_\Phi = \frac{4I_c R}{\Phi_0(1+\beta_L)}\left[1-(L/L_T)^{1/2}\right],\tag{1.7}$$

where $L_T = \Phi_0^2/4\pi k_B T$ is a temperature-dependent inductance. At 77K, $L_T = 321$ pH and the transfer function is significantly reduced for SQUID inductances above 100 pH. Koelle *et al.*[15] reformed extensive numerical simulations to explore the dependence of the high-T_c SQUID transfer function, finding Eq.(1.7) to agree with simulations for $0.09 < L/L_T < 0.35$ for $\beta_L = 1$ but to underestimate V_Φ outside this range.

The low frequency 1/f noise is generated by two separate sources: critical current fluctuations in Josephson junctions[16] and the motion of flux vortices[17] trapped in the body of the SQUID. The fluctuations in the critical current of the junctions contribute in two independent ways: an in-phase mode, in which the critical current of the junctions fluctuate in phase to produce a voltage across the SQUID, and an out-of-phase mode, in which the fluctuating critical current produces a current around the SQUID loop. Fortunately, appropriate readout schemes can eliminate both sources of noise (Sec. 3.2).

The motion of flux vortices trapped in the body of the SQUID manifests itself as a flux noise, which behaves as though an external flux noise were applied to the SQUID. The 1/f noise appears to depend strongly on the microstructure of the thin films[17]. As an example, early high-T_c dc SQUIDs made from polycrystalline YBCO[18] films exhibited high levels of 1/f noise, about 5 orders of magnitude higher in noise energy than typical

epitaxial YBCO films. Furthermore, the microstructure quality of patterned film edges is also crucial. Unfortunately, the 1/f noise due to flux motion can not be reduced by any bias reversal scheme. However, one can reduce 1/f noise due to flux motion by improving the film quality and by incorporating narrow lines in the SQUIDs and associated input circuits (Sec. 4.1).

1.4   HTS Josephson junctions

There are many methods of fabricating HTS Josephson junctions. However, there are only a few types of high-T_c junctions that meet the requirements for a successful junction technology, including a nonhysteretic I-V characteristic, a high I_cR product, high yield, good stability under room temperature storage and thermal cycling, and low 1/f noise. The most successful junction technologies for SQUIDs are bicrystal grain-boundary junctions[19], step edge grain-boundary junctions[20] and step edge SNS junctions[21] (Fig. 1-3).

Because of the high degree of anisotropy of HTS superconductors with respect to both crystal structure and transport properties, the weak coupling in the a-b plane between two superconducting grains with different orientations provides a new type of weak link. This fact has led to the development of the technologies of bicrystal grain-boundary junctions and step edge grain-boundary junctions. Of these two technologies, bicrystal grain-boundary junctions are the most straightforward. A SQUID is made by

(a) Bicrystal grain-boundary junction

(001)   (001)

Grain-boundary

(b) Step edge grain-boundary junction

(001)

(001) (001)

α

Grain-boundary

(c) Step edge SNS junction

(001)   Ag or Au

(001)

$YBa_2Cu_3O_{7-\delta}$

$YBa_2Cu_3O_{7-\delta}$

$LaAlO_3$
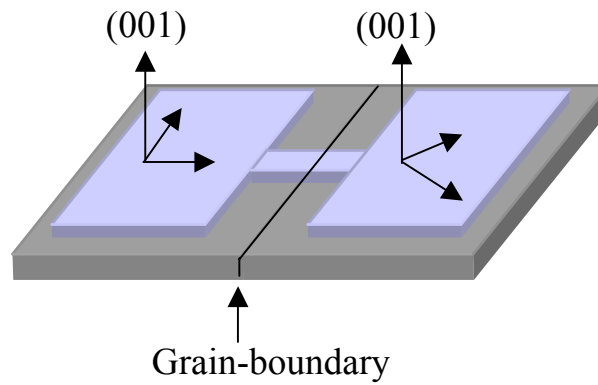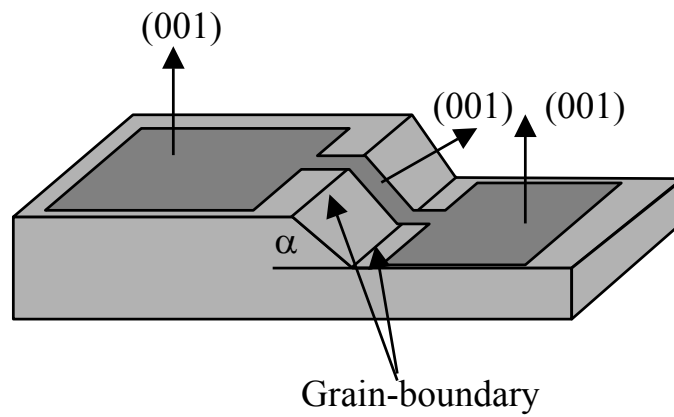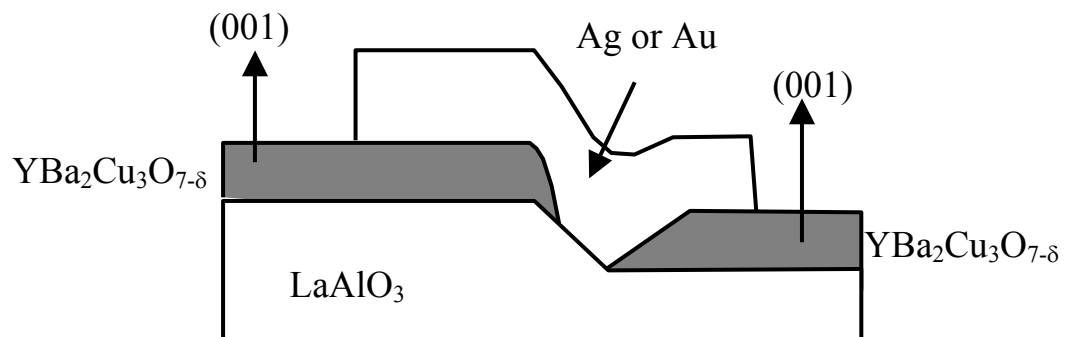
Fig. 1-3 Types of HTS Josephson junctions.

depositing an HTS superconducting film (such as YBCO) on a substrate with a misorientation angle (24° or 30°), followed by patterning narrow bridges across the boundary. This straightforward fabrication process makes these junctions the most reliable and successful currently available. However, the junction parameters often vary considerably because of variations in the quality of the grain-boundary. In addition, these bicrystals cost much more than a single crystal. Consequently, step edge grain-boundary junctions are also widely used, particularly for rf SQUIDs.

The step edge grain-boundary junction is based on the fact that an epitaxially grown, c-axis YBCO film changes its orientation at a steep step in the substrate. Therefore, one creates a steep step in a single crystal substrate, normally with an Ar ion mill, followed by YBCO deposition and patterning. Two grain-boundary junctions are formed, at the upper and lower steps. The advantage of this technology is that it enables one to fabricate more complex circuits. However, the control of the angle of the step and the microstructure of the edge are major issues, and the reproducibility is poorer than with bicrystal junctions.

The step edge SNS junction was introduced by DiIorio et al.[13]. Since the metal layer is used to connect two superconducting electrodes, the microstructure of the edge is less critical. In principle, fabrication is simple: one mills a steep step in the substrate and deposits YBCO film in a way that the film does not grow on the step. Without breaking the vacuum, one fills the gap by depositing of an Au or Ag layer, which makes contact with the two banks of the YBCO film. However, because it involves a heteroepitaxial

10

growth of the HTS film and the interlayer material, the absence of a reproducible

fabrication process has hindered the widespread use of this kind of junction.

Chapter II

Fabrication Techniques

In this chapter, I will describe the fabrication processes for making devices and the techniques for characterizing them. We use $YBa_2Cu_3O_{7-\delta}$ to make high transition temperature superconducting devices. The reasons we chose $YBa_2Cu_3O_{7-\delta}$ include its well-known physical properties, a wide variety of deposition techniques for $YBa_2Cu_3O_{7-\delta}$ films, and its high critical current density. The well-known physical properties of $YBa_2Cu_3O_{7-\delta}$ provide a good basis for selecting compatible materials and processes. A wide variety of deposition techniques enables us to produce excellent quality *in situ* thin films. The high critical current density, which can be as large as 10^7 A·cm^{-2} at 77K, is adequate for most applications.

There are several different techniques to deposit $YBa_2Cu_3O_{7-\delta}$ thin films *in situ*, such as pulsed laser deposition (PLD)[22-27], off-axis RF sputtering[28,29] and co-evaporation[30-32]. The most commonly applied to $YBa_2Cu_3O_{7-\delta}$ fabrication are PLD and rf sputtering. In Berkeley, we use the PLD system; however, MagneSensors chooses the off-axis RF sputtering system. I will describe both methods in this chapter.

2   Fabrication at UC-Berkeley

2.1.1 Pulsed Laser Deposition System

(a) equipment

We fabricated $YBa_2Cu_3O_{7-\delta}$ films with a pulsed laser deposition system, which was built by Fred Wellstood and Jack Kingston[33] about 10 years ago and has been upgraded over the years. The PLD system consists of a laser, an optical imaging system and a vacuum system, shown in Fig. 2-1 (a). We use a Lambda Physik Compex 200 excimer laser, which uses a gas mixture of F_2, Kr and Ne that needs to be replaced every month. By regulating the energy internally and using a circular aperture 7.9 mm in diameter, we obtain a uniform beam with a typical energy of about 75mJ per pulse as measured by an external energy meter prior to each film deposition.

The optical imaging system includes two planar mirrors and a planoconcave lens. All the optical elements are mounted on standard light tracks. The beam emerges from the laser, following a zigzag path that almost doubles its path and passing through the lens into the chamber. The length of the optical path is adjusted so that the beam spot is 2.5 mm wide on the target.

The stainless steel chamber contains the substrate heater block, a holder for six targets, a shutter and several feedthroughs on the walls, shown in Fig. 2-1 (b).   The

(a)
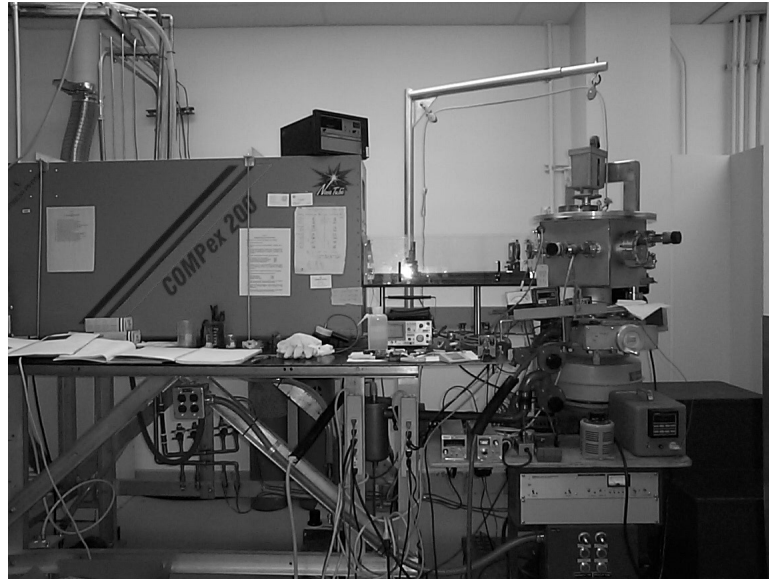
(b)
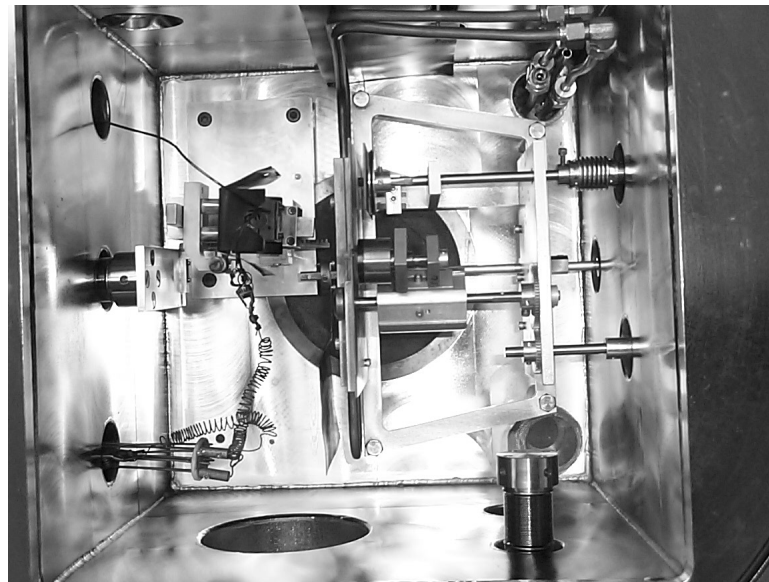
Fig. 2-1 (a) The pulsed laser system, with the laser on the left hand side, an optical imaging system at centre and the vacuum system at right. (b) Top view of the stainless steel vacuum chamber: at the left hand side is a heater block, the $YBa_2Cu_3O_{7-\delta}$ target is at right near the middle, and there is a shutter and a copper panel between them.

feedthroughs include electrical ones for the substrate heater, pressure sensors and a thermocouple, and others for O_2 flow and target rotation. In addition, there are three quartz windows: one that admits the laser beam into the chamber and others that allow us to observe the interior of the chamber.

The heater block is made of Hanes alloy with an embedded resistive cartridge heater. A stainless steel radiation shield surrounds the heater block except for the front surface where the substrate is mounted with a Hanes alloy clip. There are two kinds of clips: one with a 7 mm diameter hole is for a $SrTiO_3$ single crystal, which is 6 mm by 6 mm, and the other has clips at four corners for a 10 x 10 mm^2 bicrystal. The temperature of the heater block is regulated by a programmable Omega temperature controller, which uses the thermocouple as a temperature sensor. In addition, an infrared pyrometer, which provides a more reliable measurement of temperature than the thermocouple at low pressures, is used to monitor the blackbody radiation from a hole in the heater block. The heater block is placed on a holder that allows me to rotate the heater and change the distance between the substrate and the target. We found that 49 mm is a good distance at which only the tip of the plume touches the substrate.

The six-target system allows us to change the targets using a rotating feedthrough without breaking the vacuum. Each target, which is positioned in front of the heater block face to face, is a pressed-powder disk 25 mm in diameter and 7 mm thick. During the deposition, the target is in a contact with an O-ring on a rotating disk, which rotates the target about 60 revolutions per minute. After long usage, the O-ring wears out and

needs to be replaced. In front of the target is a water-cooled copper sheet with a rectangular opening 10 x 20 mm^2, which allows the laser beam to strike the target and the plume of the ablated material to emerge. A shutter in front of the heater block allows me to clean the target using the laser beam without depositing the material onto the substrate.

The stainless steel vacuum chamber is evacuated by a diffusion pump backed by a mechanical roughing pump. Both pumps use liquid nitrogen cold traps. The base pressure is about 2 x 10^{-6} torr. The O$_2$ pressure is regulated by throttling the gate valve and letting O$_2$ gas into the chamber through a needle valve.

(b) substrates

It is well known that the superconducting properties of the high-T$_c$ materials are highly anisotropic. To achieve a high transition temperature with YBa$_2$Cu$_3$O$_{7-\delta}$ thin films, they must have the correct crystalline structure. Besides, for a film to have a substantial critical current density, the microcrystalline structure should be free of high-angle grain boundaries. Thus, each layer must be epitaxially matched to any layer on which it grows.

There are a number of suitable substrates for growing YBa$_2$Cu$_3$O$_{7-\delta}$, including SrTiO$_3$, LaAlO$_3$, MgO and YSZ. Table 2-1 lists their crystal structure, lattice constant, thermal expansion coefficient and dielectric constant. In our own research, we use (100) SrTiO$_3$ substrates because the lattice constant closely matches that of YBa$_2$Cu$_3$O$_{7-\delta}$.

Table 2-1 Parameters of YBCO and selected substrates

Material	Structure	Lattice constant (Å)	Thermal expansion coefficient ($10^{-6}/^oC$)	dielectric constant at 25^oC
$YBa_2Cu_3O_{7-\delta}$	orthorhombic	a = 3.83 b = 3.89 c = 11.7	8.5	-----
$SrTiO_3$	cubic	3.905	9.4	> 300
MgO	cubic	4.213	14	10
YSZ	cubic	5.147	11	27
$LaAlO_3$	f.c. orthorhombic	7.580 $\alpha \approx 90.5^o$	9.8	26

In addition, we use 30° SrTiO$_3$ bicrystal substrates to make SQUIDs. Since the unit price of a bicrystal is much more than that of a single crystal, we optimize our deposition process for YBa$_2$Cu$_3$O$_{7-\delta}$ films on SrTiO$_3$ single crystals and then use it for bicrystals. Normally, we make at least a dozen SQUIDs on one 10mm x 10mm bicrystal and choose the best ones to use.

(c) procedure

The procedure described in this section is the standard process for depositing YBa$_2$Cu$_3$O$_{7-\delta}$ films on substrates in Berkeley. To enable us to see the grain boundary under the microscope of the mask aligner, the bicrystal is etched with hydrofluoric (HF) acid before depositing the YBa$_2$Cu$_3$O$_{7-\delta}$ film. We spin photoresist onto the surface of a new bicrystal and pattern a photomask that covers the entire surface except for two windows, about 0.5 mm x 0.5 mm, at the outer edges of the grain boundary. The bicrystal is immersed in a 9% aqueous solution of HF acid which etches along the exposed grain boundary. Typically, we etch for about 20 seconds and wash the HF acid away with disionized (DI) water for 10 seconds. Figure 2-2 shows the etched grain boundary. The etched grain boundary remains visible even after YBa$_2$Cu$_3$O$_{7-\delta}$ is deposited. The photoresist is removed by spraying the surface with acetone followed by ultrasound in a beaker of acetone, isopropanol and methanol, each for 3 minutes. Shortly after it is taken out of the beaker of methanol, the substrate is blown dry with compressed

100 μm
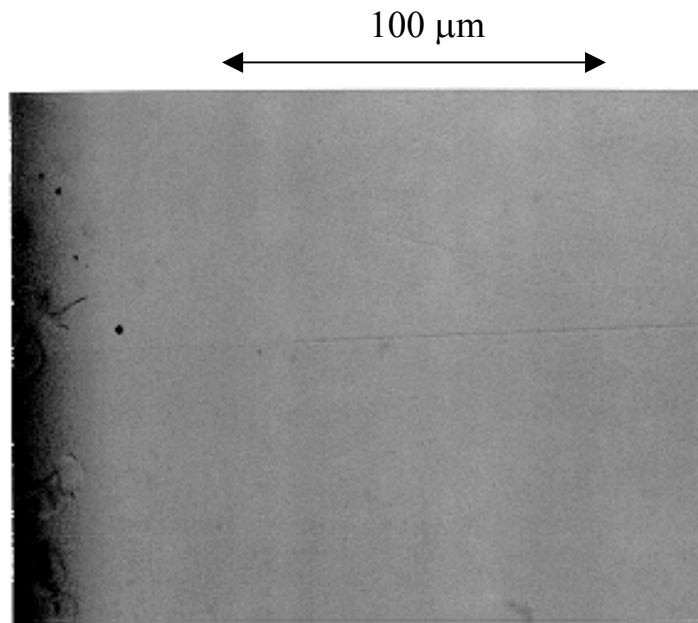
Fig. 2-2 Photograph of HF etched grain boundary.

N_2 gas, and then kept in a desiccator. However, if the substrate is a single crystal, we do not do the HF etch.

To clean the chamber, we often start by removing the heater block and the $YBa_2Cu_3O_{7-\delta}$ target from the chamber. The Hanes alloy heater block and the clip are wire-brushed in the student machine shop before mounting the substrate. It is important to have a flat surface on the heater block for good thermal contact.

The $YBa_2Cu_3O_{7-\delta}$ target is polished with sandpaper in three steps, with grit numbers 300, 600 and 1200. The coarse sandpapers, grit 300 and 600, remove the laser markings from the previous deposition and the fine sandpaper polishes the target to get a shining surface. we then blow the target with 20 psi compressed N_2 gas and press the target against a new glove to remove any particles on the surface. The vacuum chamber is cleaned thoroughly by wiping the chamber with methanol to remove any $YBa_2Cu_3O_{7-\delta}$ from the previous deposition, especially the fixtures between the target and the substrate. However, after many depositions, say 30 or so, the chamber becomes so dirty that we cannot clean the chamber with methanol. we then remove some parts from the chamber and clean them and the chamber with 10% HNO_3 in DI water followed by methanol. If the target exhibited an electrical discharge during the previous deposition, we would clean the chamber with 10% HNO_3 in DI water followed by methanol, without taking parts out of the chamber. A clean chamber is the key to making a good quality $YBa_2Cu_3O_{7-\delta}$ film.

The substrate is cleaned in the following steps, starting in a beaker of Trichloroethane (TCA) for 3 minutes in an ultrasonic bath to remove any residual wax and dirt, followed by acetone, isopropanol and methanol. We then blow it dry with compressed N_2 gas. Note that if the substrate is a bicrystal, we usually hold the beaker during the ultrasonic cleaning to reduce the force on it. The cleaned substrate is then inspected under an optical microscope for any remaining contaminants and the methanol cleaning step is repeated if necessary.

A silver foil is cut so that its size is a little bit larger than that of the substrate, 2 - 3 mm larger than the width or the length of the substrate. The silver foil, the clip and two screws are cleaned in a beaker of acetone in an ultrasonic bath for 3 minutes, followed by isopropanol and methanol. The heater block is wiped with acetone, isopropanol and methanol. To mount the substrate on the heater block, we first apply a certain amount of silver paste uniformly on the silver foil and press the substrate to the silver foil to get good contact between them. Note that the silver paste should not be applied too thickly so that it flows over the edges of the substrate onto the surface. The combination of the silver foil and the substrate is then mounted on the heater block using the clip with two screws. It is necessary to tighten the screws evenly and gently, to assure good thermal contact and to prevent breaking the substrate from too much applied force. The thermal contact between the heater block and the substrate is the most crucial element for making $YBa_2Cu_3O_{7-\delta}$ thin films. We then use a Halogen lamp to bake the silver paste for 15 minutes. We normally re-tighten the screws a bit more after baking and blow N_2 gas over the substrate. The heater block is now ready to install to the chamber.

While baking the silver paste, we usually fill cold traps with liquid nitrogen, place the target in the chamber and check the rotation of the target. We then place the heater block in the chamber and make sure that the surface of the heater block is parallel to the copper panel in front of the target. The current leads and a thermocouple are attached to the heater. We check the heater by measuring its resistance, about 37 Ω. The shutter should be in a position to block the plume completely, while making room available for the laser to strike the target.

After double-checking the target rotation and the shutter position, We pump the chamber down to 2 x 10^{-6} torr. We then heat the substrate from room temperature to 810°C (measured with the infrared pyrometer) in 30 – 40 minutes. The temperature controller is programmed to raise the temperature from room temperature to 780°C in 20 minutes. However, we keep the output power to less than 80% during heating, and when the temperature reaches 780°C, we readjust the regulator so that the temperature of the heater block measured by the pyrometer is 810°C. The optimal deposition temperature is based on results from the test films. While heating the substrate, we put on laser safety goggles, turn on the laser and run it at 1 Hz into an external energy meter placed in front of the laser output. We adjust the internal laser energy so that the energy through the aperture is 75 mJ per pulse (25 mV per pulse from the oscilloscope).

After the temperature is stable, we rotate the heater block so that we can see the color of the substrate, which should be a uniform bright red, to make sure it has good thermal contact. In addition, an infrared pyrometer is used to check the temperature

during the deposition. The chamber pressure is then regulated to 210 mT in O_2 by throttling the gate valve and letting O_2 gas through a needle valve which is controlled by a pressure gauge. The temperature is re-adjusted to $810^{o}C$ if necessary. We then move the target into position, start the rotation, close the shutter, put on the laser safety glasses and fire the laser at the rotating target at 10 Hz for 1 minute to clean the surface of the target. After 1 minute, we close the laser shutter, open the substrate shutter, reset the laser to 5 Hz, check the temperature, pressure and rotation, and re-open the laser shutter to deposit the $YBa_2Cu_3O_{7-\delta}$ film. During the deposition, only the tip of the plume touches the substrate. A 160 – 200 nm thick $YBa_2Cu_3O_{7-\delta}$ film is deposited in about 12 minutes.

When the deposition is complete, we close the laser shutter, change the O_2 pressure to 250 mT immediately, reduce the temperature to $780^{o}C$, turn off the laser power and stop the target rotation. Once the temperature and the pressure are stable, we close the gate valve completely and let in 550 torr of O_2 while the temperature is stabilized at $780^{o}C$. The substrate is then cooled to $450^{o}C$ in 20 minutes, regulated by the temperature controller. At the end of the cycle the heater power is shut off, and the substrate is cooled to room temperature in about an hour. We then remove the substrate from the heater block very carefully with one hand holding the heater block steadily and the other hand holding a new razor blade to separate the substrate and the heater block gently. Normally, we would start from four corners with the blade horizontally. Note that if the blade is not parallel to the substrate, the substrate is stressed and may break. A thin layer of silver film is deposited onto the $YBa_2Cu_3O_{7-\delta}$ film in another chamber

immediately. The laser deposition chamber is pumped with a diffusion pump for few minutes and filled with 550 torr of O_2.

2.1.2 Thermal Evaporation

It is well known that contact pads, silver film, should be deposited onto a freshly deposited $YBa_2Cu_3O_{7-\delta}$ film to reduce the contact resistance between the silver film and $YBa_2Cu_3O_{7-\delta}$ film. We deposit silver films by thermal evaporation, using a Varian Model 3118 Evaporator with a quartz crystal monitor to measure the film thickness during each deposition.

After a $YBa_2Cu_3O_{7-\delta}$ film is taken out of laser deposition chamber, it is attached to a glass slide with double-stick tape and partially covered by aluminum foil which serves as a shadow mask. The film is placed face down on the top of the sample holder, and silver pellets are placed in a boat near the bottom of the chamber. After the chamber is pumped down to a pressure of 2×10^{-6} torr, the silver is thermally evaporated onto the $YBa_2Cu_3O_{7-\delta}$ film at a rate of 0.25 nm per second. Typically, we evaporate 100 nm of silver, which covers the area of the film where the contact pads will be patterned.

2.1.3 Patterning

We pattern our devices in the Berkeley Microfabrication lab (microlab), which is a class 100 clean room. Before going to the microlab, we usually clean the film in a

beaker of methanol in an ultrasonic bath. In the microlab, we start by spinning Shipley 1818 (S1818) photoresist onto the film at 6000 rpm for 30 seconds and baking the photoresist on a hot plate at 90°C for 5 minutes. Our masks are laid out using a CAD program and transferred to emulsion or chrome plates. We align the SQUID mask over the bicrystal using a Canon 4X Projection Mask Aligner, which allows us to pattern structures as small as 1 μm. There are many alignment marks on the outer edges of the mask. By aligning the etched grain boundary to those alignment marks, we ensure that the SQUID junctions will lie on the grain boundary. The photoresist is developed in a 1:1 solution of Microdeposit Developer Concentrate and DI water with agitation for about 10 seconds, followed by DI water for 5 seconds, and blown dry. The developing time depends on the exposure time. We often try different combinations of exposure time and developing time on test chips before patterning bicrystals. Typically, for a SQUID pattern which has silver pads some distance away from the junctions, we use an exposure time of 6.0 or 6.2 in the Canon, and the developing time is 8 to 10 seconds.

However, when we pattern a YBa$_2$Cu$_3$O$_{7-\delta}$ flux transformer on a 4-inch wafer, we spin Shipley 1818 (S1818) photoresist onto the film at 4000 rpm for 30 seconds and bake at 70°C for 4 minutes. Because the wafer is too large to place under the Canon mask aligner, we use the Quintel Contact Aligner to pattern the flux transformer. The exposure time depends on the UV light energy density, which varies from day to day. Therefore, we calibrate the energy density before we pattern the film. The developing time is somewhat longer than that for bicrystals, typically 30 seconds.

2.1.4 Ion Milling and Acid Etch

There are two techniques used in Berkeley to etch $YBa_2Cu_3O_{7-\delta}$ films. The ion mill is a convenient dry etching technique. Its main advantage is the ability to mill films at an arbitrary angle, which is important for making edges with well-defined bend angles . Another technique is acid etch, a wet etch technique, which is good for large size wafers that cannot be placed in the ion milling chamber.

Our ion mill system consists of a vacuum system, an ion source, a neutralizer and a water-cooled sample stage. The vacuum system contains a stainless steel vacuum chamber that is pumped by a cryopump. The chamber has two glass windows that allow us to observe the progress of the ion milling.

We use a Nordiko 5 cm RF Ion Source to generate the Ar ion beam. The ion source is operated at an accelerating voltage of about 500 V to generate a beam current of 120-180 μA per cm^2. A Nordiko rf neutralizer is also mounted inside the chamber to supply a beam of electrons at about 70° to the ion beam to prevent the ions from charging up the dielectric substrate.

The sample stage is screwed to a copper block connected to a shaft that can be rotated from outside the chamber using a feedthrough. Therefore, the sample can be rotated with respect to the ion beam so that the film can be milled at any angle to the substrate. However, we usually mill samples at normal incidence. The copper block

contains a U-shaped copper tube, which extends outside the chamber and is immersed in an ice bucket, to enable us to flow chilled water to cool the block. The sample stage is in thermal contact with the copper block through heat-conducting vacuum grease. The sample is glued to the stage with heat-sink compound as well as a little vacuum grease. A shutter is used to stop the ion milling for a short time.

Once the film is patterned, we place the sample in the chamber and pump the chamber down to 2×10^{-6} torr. To prevent overheating the sample, we usually mill the film for 2 minutes and close the shutter for 1 minute; meanwhile the chilled water keeps flowing through the copper tube. A 200 nm thick $YBa_2Cu_3O_{7-\delta}$ film takes about 20 minutes to etch away. During the milling, we always make sure that the copper tube is immersed in the ice completely. After taking the sample out of the chamber, we remove the photoresist and heat-sink compound with acetone in an ultrasonic bath, spray an isopropanol and methanol, and blow the film dry with N_2 gas.

To pattern a $YBa_2Cu_3O_{7-\delta}$ flux transformer on a 4 inch sapphire substrate, we use chemical wet etching. Typically, we use a 0.05% aqueous solution of HNO_3 followed by DI water which removes residual nitric acid. The etching rate depends on the thickness of the film. Note that the wet etching produces undercutting, shown in Fig. 2-3. It means that one has to control the etching time carefully when patterning small features.
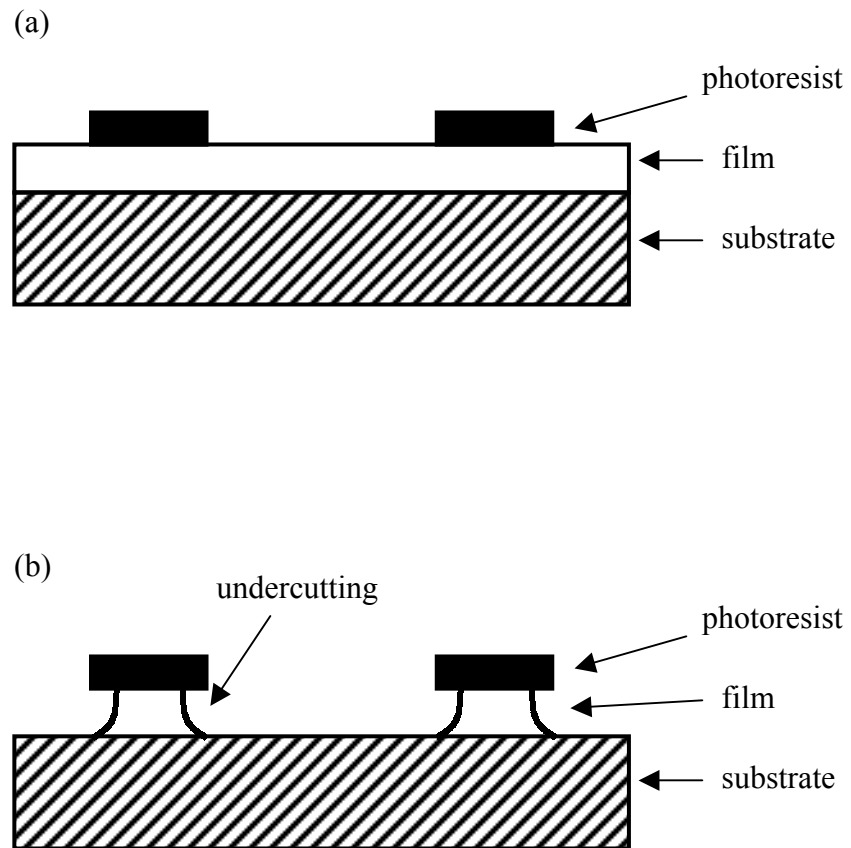
Fig. 2-3 (a) Sample before wet chemical etching; (b) sample after wet chemical etching.

2.2 Fabrication at MagneSensors Inc.

Both step edge SNS SQUIDs and multilayer flux transformers are fabricated by MagneSensors Inc., San Diego, CA. Details of their processes are published elsewhere[34,35] Here I briefly describe the SNS junction and multilayer techniques.

The SNS junction fabrication process starts by producing a sharp step on a $LaAlO_3$ substrate with an ion mill using a Nb mask to help sharpen its profile. Typically, the step height is 150-250 nm. A 150-200 nm thick $YBa_2Cu_3O_{7-\delta}$ film is deposited onto the etched substrate with an off-axis RF sputtering system, followed by the sputter deposition of Ag-Au alloy normal metal, without breaking vacuum, shown in Fig.2-4. The step height and the thickness of the $YBa_2Cu_3O_{7-\delta}$ film are chosen so that the gap between the $YBa_2Cu_3O_{7-\delta}$ banks is on the order of the normal metal coherence length. Hence, the two superconducting banks are coupled via the proximity effect. Following the film deposition, the film is processed using standard photolithography and ion-beam etching, which is similar to the processes described in sections 2.1.3 and 2.1.4.

Two types of multilayer flux transformers are made: without flux dams and with flux dams in the pickup loops. The basic multilayer $YBa_2Cu_3O_{7-\delta}$-$SrTiO_3$-$YBa_2Cu_3O_{7-\delta}$ process is the same for both types of flux transformers. To create flux dams, MagneSensors simply uses SNS junctions that have high critical currents. All the films are deposited with off-axis sputtering.
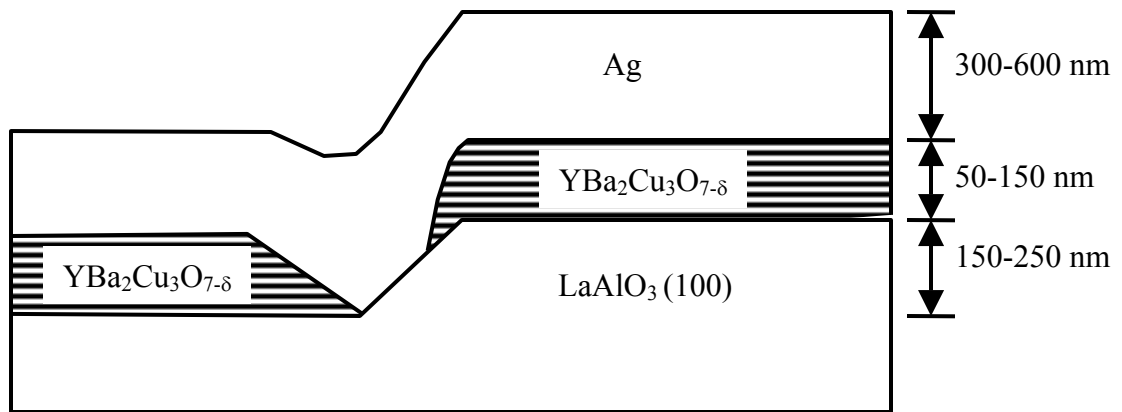
Fig. 2-4 Schematic drawing of the SNS Josephson junction structure.

The multilayer YBCO-STO-YBCO process begins with $YBa_2Cu_3O_{7-\delta}$ deposition on a $LaAlO_3$ substrate. The ion mill is performed at a 45° angle in order to bevel the edges of $YBa_2Cu_3O_{7-\delta}$ film. The $SrTiO_3$ insulator then coveres the underlying $YBa_2Cu_3O_{7-\delta}$ film completely. In order to grow a good quality $YBa_2Cu_3O_{7-\delta}$ film on $SrTiO_3$, it is important to produce smooth films of both the bottom layer $YBa_2Cu_3O_{7-\delta}$ and the $SrTiO_3$. The via holes in the $SrTiO_3$, which enable contact from pickup loop, top layer $YBa_2Cu_3O_{7-\delta}$ film, to the innermost coil turn, bottom layer $YBa_2Cu_3O_{7-\delta}$ film, are beveled during the ion milling to facilitate a superconducting contact. Finally, the top layer $YBa_2Cu_3O_{7-\delta}$ film is deposited on the $SrTiO_3$ and patterned to form pickup loops.

2.3 Characterization of YBCO Films

In order to know if we have a good fabrication process for $YBa_2Cu_3O_{7-\delta}$, we pattern the $YBa_2Cu_3O_{7-\delta}$ films on $SrTiO_3$ on single crystals into bridges with widths of 2 μm, 4μm and 8 μm. To calibrate the films, we measure their resistances during cooling and their critical current densities at liquid nitrogen, 77K. The setup includes a probe, a cryostat and several electronic devices. The probe contains a Pt thermocouple and a 68 pin chip carrier. The Pt thermocouple allows us to record the temperature while cooling. To obtain an accurate temperature reading of the sample, we mount the thermocouple on the reverse side of the carrier. The 68 gold contacts enable us to measure all bridges on a single crystal in one cooling step. The sample is glued to the carrier with rubber cement. The electrical contact between Ag-covered contact pads on the films and the gold pads on

the carrier is made by ultrasonic bonding 25 μm diameter aluminum wires. The probe is cooled by inserting it into a fiberglass dewar surrounded by a high permeability (μ-metal) shield.

A current source, an HP multimeter and a Lakeshore temperature controller are used to measure the resistance and to record the temperature simultaneously. The current source is simply a combination of a 1.5 V battery and several resistors, which produces a 100 μA current in the sample. The HP multimeter is used to measure the voltage across the bridges. The temperature controller reads the temperature from the Pt thermocouple. Both the HP multimeter and the temperature controller are connected to a computer and operated by a Labview program which enables us to plot resistance (R) vs. temperature (T) during the measurement.

Figure 2-5 shows a typical R-T curve. The resistance of a good quality $YBa_2Cu_3O_{7-\delta}$ film should decrease linearly with temperature. At the transition temperature the resistance decreases dramatically to zero, typically with a width of less than 2K. The extrapolation of the normal state resistance should extend to zero at zero temperature.

The critical current measurement involves a function generator, a current-voltage (I-V) box and an oscilloscope. The function generator supplies a low frequency current to a bridge. The I-V box amplifies the voltage across the bridge. Both current and
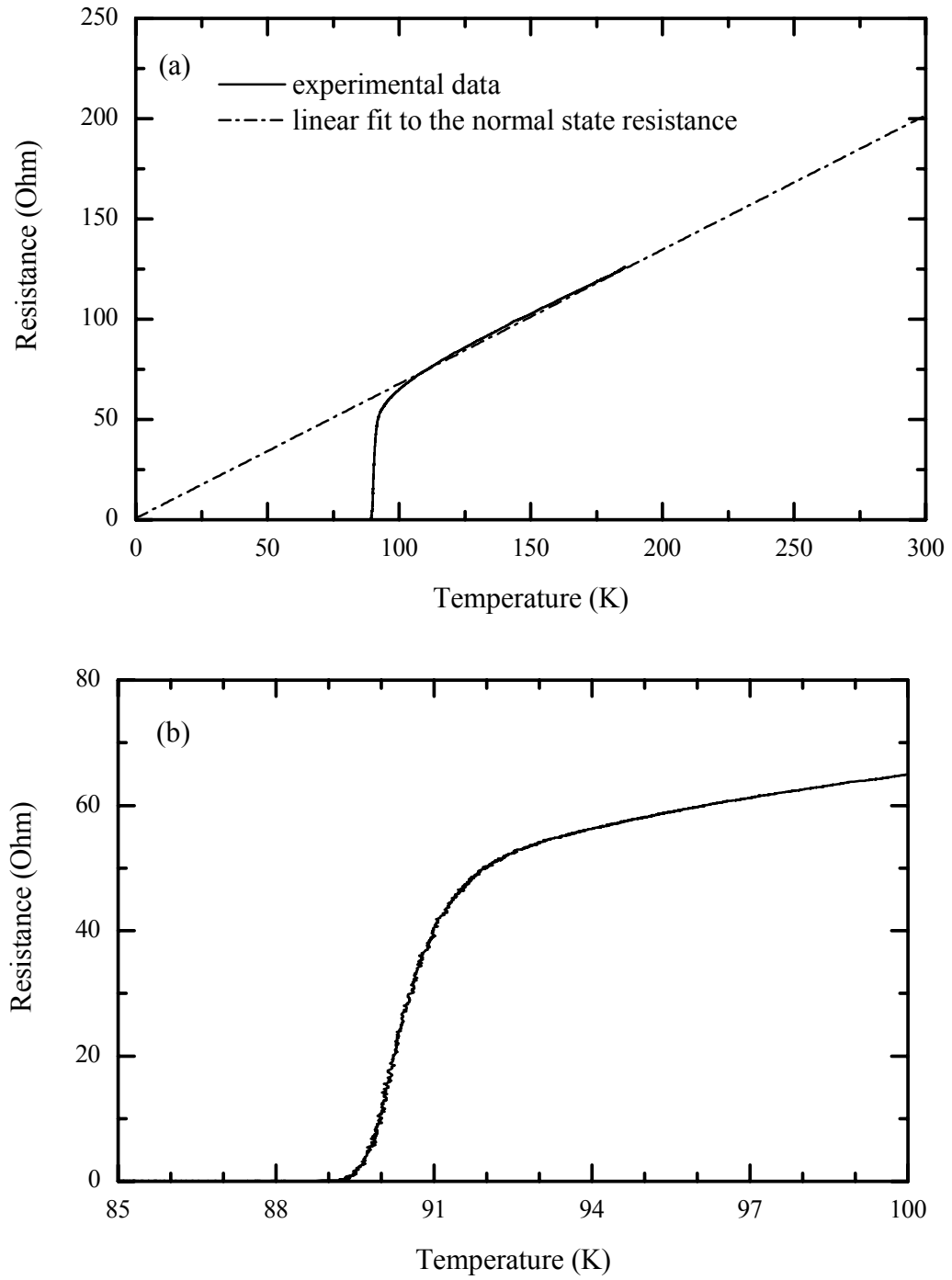
Fig. 2-5 A typical R-T curve for a 2 μm bridge: (a) extrapolation (dash line) goes to zero resistance at zero temperature; (b) enlarged plot near the transition temperature.

voltage are observed by the oscilloscope. Typically, YBa$_2$Cu$_3$O$_{7-\delta}$ films made at UC-Berkeley have a critical current density of about 5×10^6 A/cm^2.

Chapter III

Characterization of SQUIDs

The techniques we use to characterize SQUIDs at UC-Berkeley are described in this chapter. I start by describing measurements of the current-voltage (I-V) characteristics and transfer function of a SQUID, followed by the principle of operating the SQUID in a flux-locked loop and measuring its noise.

2.4   Current-Voltage Characteristics and Transfer Function

Once SQUIDs are made, we measure their critical currents, I_c, normal state resistances, R_n, and transfer functions, V_Φ. To expedite these measurement, we often use the 68 pin probe described in section 2.3. The SQUID chip is mounted on the 68 pin chip carrier and all the SQUIDs are wire bonded in one operation. A square modulation coil is placed on the carrier to provide a magnetic field. The probe is immersed in a liquid nitrogen dewar surrounded by three concentric mu-metal shields. we then measure the I-V and V-Φ characteristics of each SQUID in turn.

We use the same apparatus for measuring the critical current of a bridge to measure the critical currents and normal resistances of SQUIDs. The transfer function of a SQUID is measured by applying a current to the modulation coil, which is inductively coupled to the SQUID, monitoring the voltage across the junctions and applying a static

bias current to the SQUID slowly. The voltage across a SQUID is modulated with the applied magnetic flux with a period of one flux quantum, Φ_0. The amplitude of the voltage depends on the bias current. Therefore, we increase the static bias current slowly to achieve the maximum value of the transfer function. This simple procedure allows me to select a SQUID with the best parameters for subsequent experiments.

3.2 SQUID Readout Scheme

Although a dc SQUID is a very sensitive flux-voltage transducer for many applications, it would not be a practical device because its voltage response to flux is not linear. The voltage across the SQUID oscillates with flux with a period Φ_0, which limits its dynamic range to $\Phi \leq \Phi_0/2$. To extend its linear operating range, the SQUID is operated in a flux-locked loop in which the voltage change across the SQUID induced by an applied flux is fed back to cancel out the flux. The feedback current is read out and is linear in the flux applied to the SQUID. As a result, the flux-locked loop provides a means of measuring the intrinsic noise of the SQUID, and extends the dynamic range of the SQUID to quantities much larger than Φ_0. A flux modulation scheme[36] is most commonly used. The flux modulation scheme of a flux-locked loop is shown in Fig. 3-1.

The oscillator applies a sinusoidal or square-wave flux modulation to the SQUID with peak-to-peak amplitude of $\Phi_0/2$ at frequency f_m, typically between 100-1000kHz.
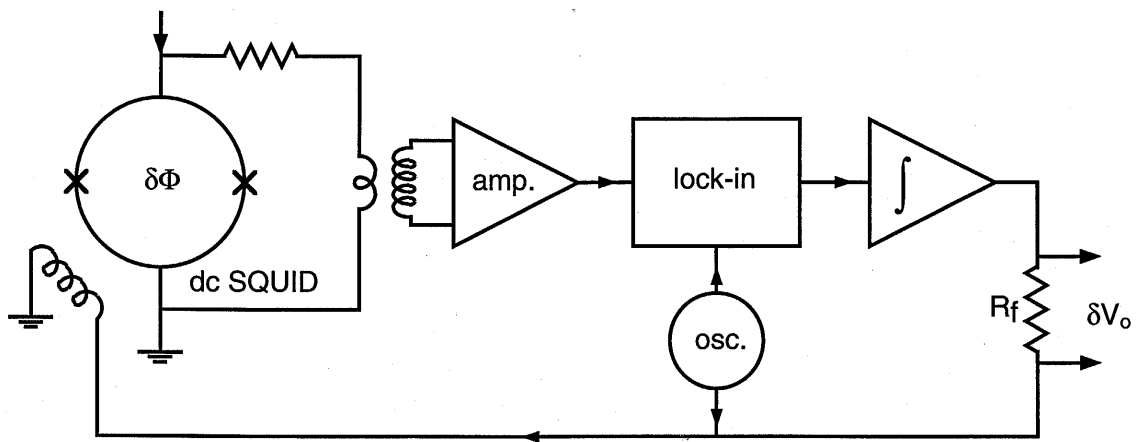
Fig. 3-1 Flux-locked loop for a dc SQUID.

The alternating voltage across the SQUID is amplified by a transformer followed by an amplifier. After the amplification, the signal is lock-in detected at the frequency f_m. If the SQUID is operated at a local maximum or a local minimum of the V-Φ curve, the voltage response contain components only at frequency $2f_m$. The output of the lock-in detector is zero. On the other hand, the modulated voltage contains a component at frequency f_m if the flux is shifted away from the minimum or the maximum, shown in Fig. 3-2. After integration, this signal is fed back as a current through a resistor R_f to the modulation/feedback coil inductively coupled to the SQUID. Thus the SQUID response is nulled out since the feedback flux opposes the applied flux. The voltage across R_f is proportional to the applied flux. Note that the SQUID detects only the difference in flux not the absolute flux. In addition, one can measure the intrinsic noise of the SQUID by connecting the output voltage to a spectrum analyzer. However, the bandwidth which the SQUID can be read out is limited to $f_m/2$ at most. For some applications where the signal is at high frequencies (a few MHz) but low frequencies are not important, for example NMR, other read out schemes are used[37]. For unshielded applications where the SQUID is exposed to the ambient magnetic field, an important issue is slew rate, the maximum rate of change of flux that the system is able to track without losing lock. Typically, this is 10^6 $\Phi_0 s^{-1}$.

A bias-reversal scheme is used to eliminate the 1/f noise due to critical current fluctuation in HTS SQUIDs. The bias-reversal scheme, which we briefly describe here, is based on that of Koch *et al.*[38]; the principle is illustrated in Fig. 3-3. Basically, the SQUID is operated in a flux-modulated flux-locked loop. The flux is modulated at a

(a)

(b)
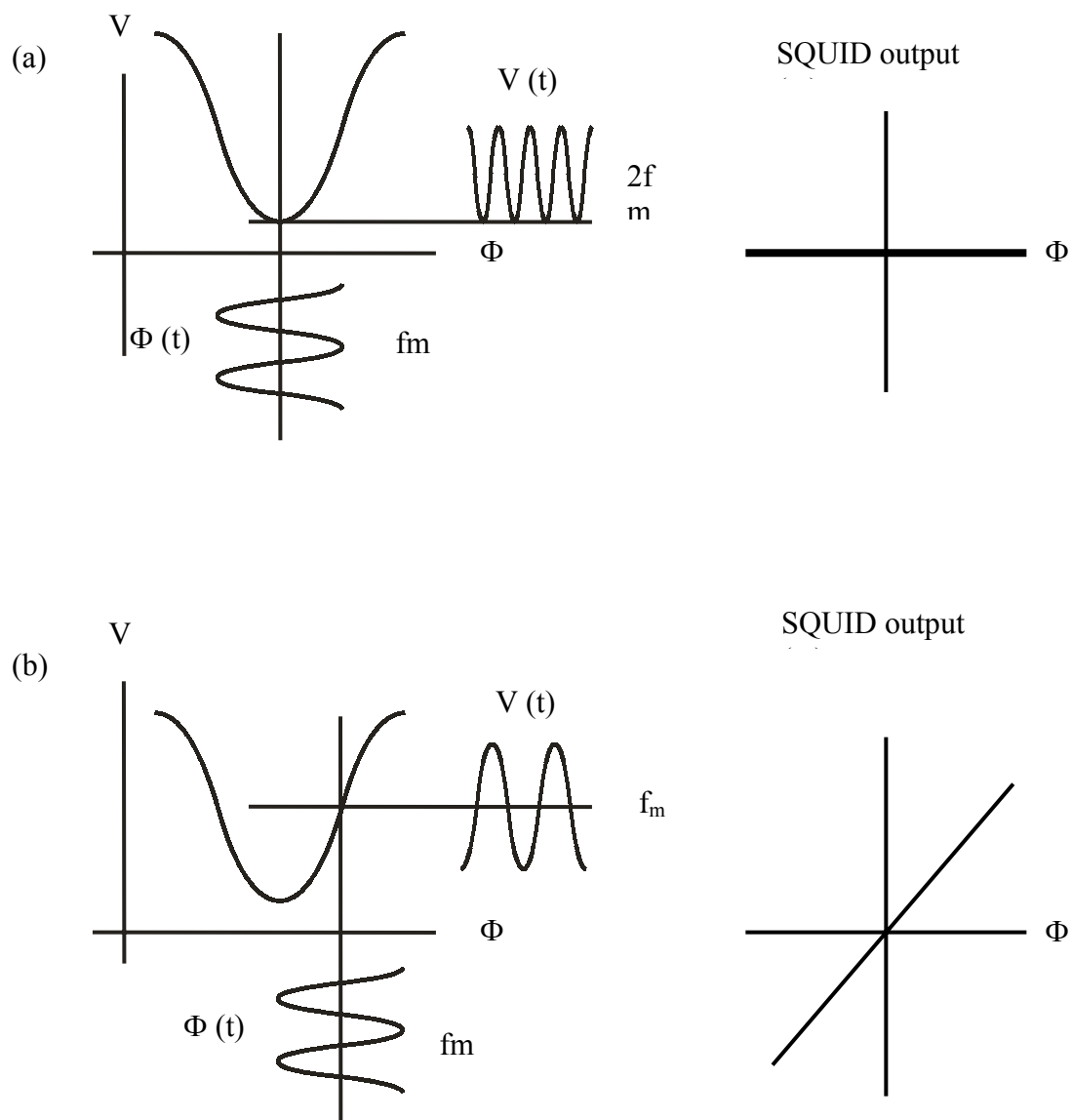
Fig. 3-2 Flux modulation
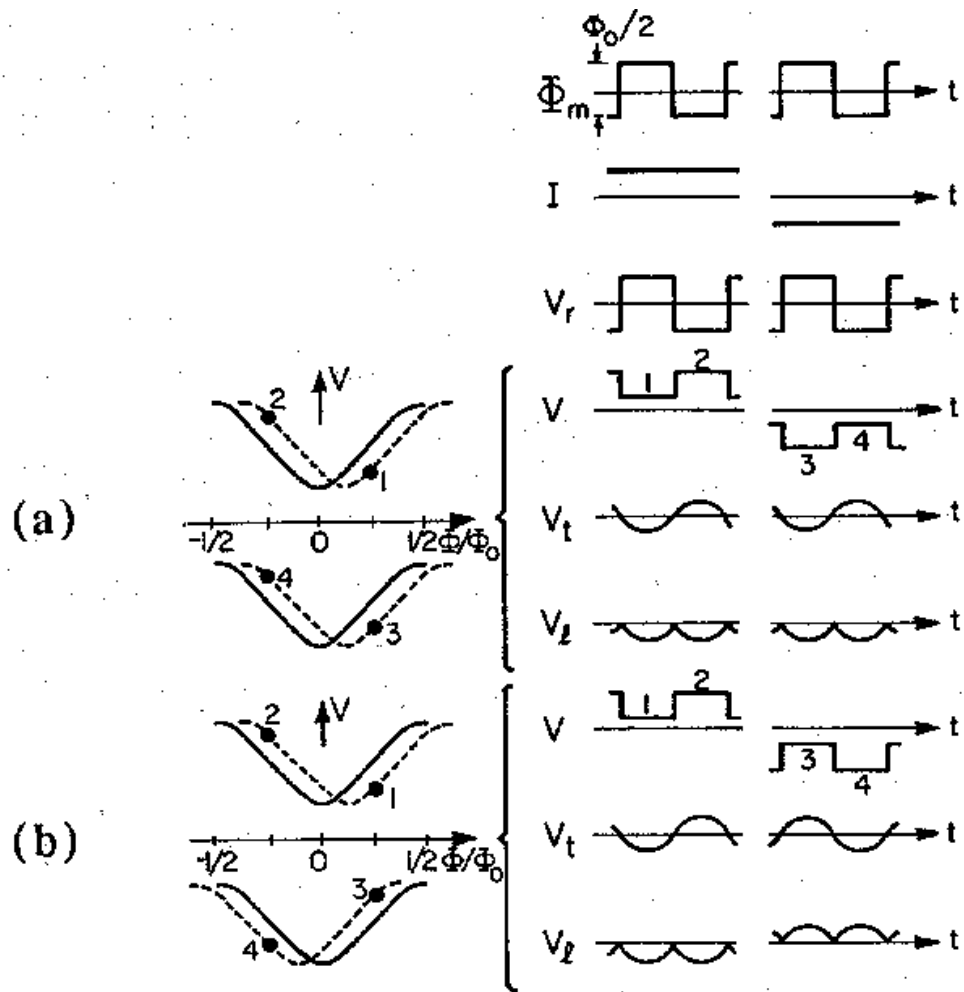
Fig. 3-3 Principle of bias-reversal scheme. The left-hand column shows the V-Φ curves (solid lines), and the dashed line indicates (a) an external flux change δΦ and (b) a flux change generated by out-of-phase critical current fluctuations. The right-hand column shows (top to bottom) the flux modulation, the bias current, and the reference voltage used to lock-in detect the signal from the SQUID; the next three rows are voltages for external flux change δΦ; the last three rows shows the voltages for an out-of-phase critical current fluctuation.

frequency f_m with peak-to-peak amplitude $\Phi_m = \Phi_0/2$. Instead of using a dc bias, the bias current through the SQUID is reversed with a frequency f_r, typically a few KHz. Simultaneously with the bias reversal, a flux $\Phi_0/2$ is applied to the SQUID. Figures 3-3 (a) and (b) show that the bias reversal changes the sign of the voltage across the SQUID while the flux shift assures that the sign of the flux-to voltage (solid lines) remains the same. As a result, the output from the lock-in detector can be integrated and fed back to the SQUID in the usual way. If we apply a small external flux $\delta\Phi$ to the SQUID at a frequency well below f_r, the V-Φ curves are shifted as the dashed lines in Fig. 3-3 (a). The flux modulation switches the SQUID between the points 1 and 2 for positive bias and points 3 and 4 for negative bias. Thus, the output from the lock-in detector V_l will consist of negative-going peaks for both polarities of the bias current. The average of this output produces a negative signal to cancel the flux applied to the SQUID. Accordingly, the SQUID responds to an applied flux in the usual way in the presence of bias reversal and flux shift.

Now suppose that we have an out-of-phase critical current fluctuation at a frequency below f_r. Because the flux generated by this current fluctuation changes sign when the bias is reversed, the V-Φ curves are displaced in opposite directions as shown as dashed lines in Fig. 3-3 (b). As a result, the voltage from the lock-in detector changes sign each time the bias current is reversed, and the average of the signal over periods much longer than $1/f_r$ is zero. Therefore, the 1/f noise due to out-of-phase critical current fluctuations is eliminated by this bias reversal scheme.

41

3.3 Noise in Zero Field and Effective Area

To measure the noise of SQUIDs and their effective areas, we use a noise probe inserted into a fiber glass dewar surrounded by three mu-metal shields. A set of commercial electronics, Conductus PCI 1000 SQUID controller, is used to operate the SQUIDs, and a HP spectrum analyzer is used to record the noise spectrum. Both the Conductus SQUID controller and the spectrum analyzer are controlled by a computer.

The noise probe is 1m long and involves a stainless steel rod with an O-ring Quick-Connect seal that allows one to adjust it at any level in the dewar. At the bottom end, the rod is attached to a G-10 fiberglass block which allows us to mount SQUIDs, and to attach a HTS tube, a solenoid, and a mu-metal can, shown in Fig. 3-4. The probe can accommodate up to four SQUIDs at the same time. The SQUIDs are mounted on a home-made chip carrier made from printed circuit board and hermetically sealed in the SQUID cavity. The cavity in which the SQUIDs are mounted contains two modulation coils and a heater. The two modulation coils allow us to operate SQUIDs with a variety of effective areas. The heater is placed above the modulation coils, and is made of a twisted pair of manganin wires embedded in two-component epoxy, Stycast 1066. All copper wires in the probe are twisted pairs. Each pair is encased in Teflon tubing and surrounded by a grounded CuNi tube to prevent cross talk and to exclude external rf noise.
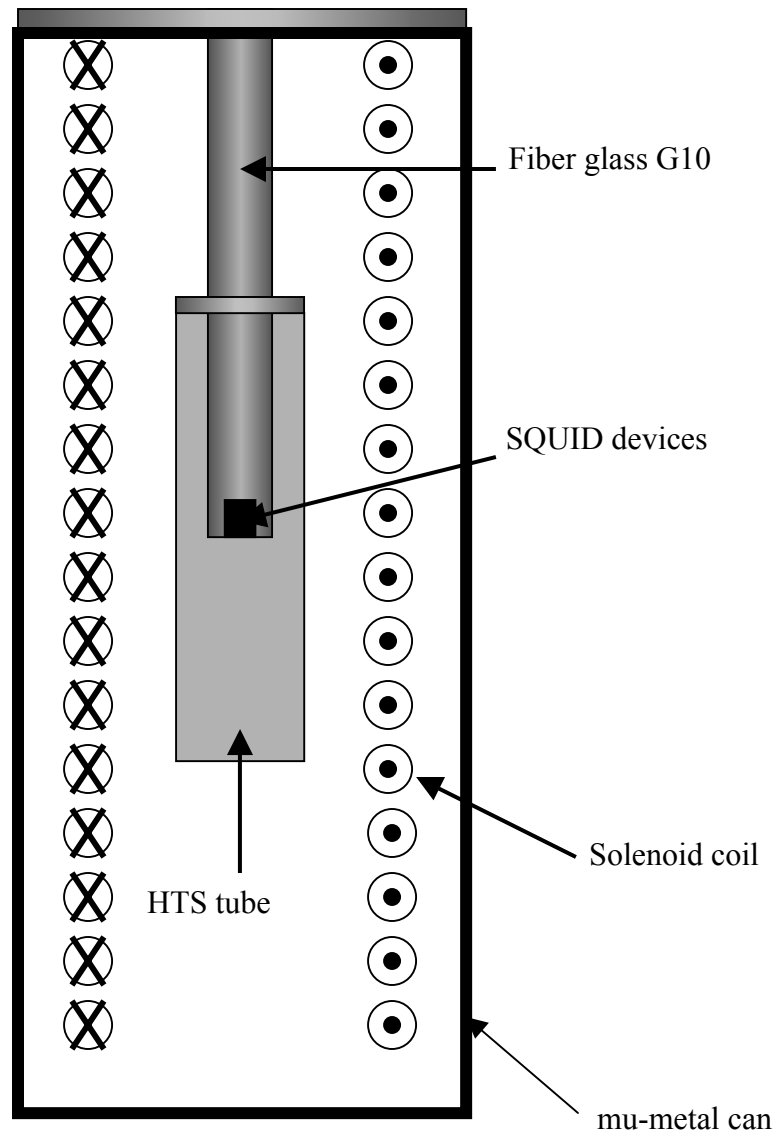
Fig. 3-4 Schematic drawing of the bottom end of the noise probe.

A solenoid 0.2m long is used to provide a uniform magnetic field. In addition to the mu-metal shields outside the dewar, a 0.1m long HTS tube and a 0.22m long mu-metal can are often used. The HTS tube is made of a thick film of $YBa_2Cu_3O_{7-\delta}$ depositing on a YSZ tube[39]. At the top end of the rod is a Pomona shielded box, which contains four BNC connectors for external magnetic field current supplies, and four LIMO connectors that are connected to the Conductus PFL. The whole probe is inserted in a fiber glass dewar surrounded by three mu-metal shields. If the HTS tube is mounted, we normally cool the SQUIDs at a very slow rate, from room temperature to 77K in about an hour, to minimize the stress in the HTS tube during cooling.

The Conductus PCI 1000 SQUID controller enables us to control the Conductus Programmable Feedback Loop Model PFL-100 with a computer. The PFL-100 is used to operate SQUIDs with a 128 kHz flux modulation and a 2 kHz bias reversal scheme. The output signal of the SQUID is monitored by an oscilloscope and a HP spectrum analyzer. The noise power spectra and the time traces are downloaded into a computer with a labview program. In practice, we usually thermal cycle the SQUIDs using Conductus electronics before we measure the noise. Note that the heating time can be set to ensure that the SQUID has been heated to its normal state. It is important to keep the heating time short because over-heating the cavity may result in vaporizing the rubber cement and its vapor can damage the YBCO film. Typically, we maintain the SQUIDs in the normal state for ten seconds; we can determine when the SQUID is normal from the output of the electronics.

The effective area of the SQUID is defined as the flux quantum Φ_0 divided by the applied magnetic field required to produce one flux quantum in each SQUID configuration. To measure the effective area of the SQUID, we simply measure the SQUID output while applying a small uniform magnetic field with the solenoid.

Chapter IV
Noise in Magnetic Fields

For a number of practical applications of high transition temperature SQUIDs, it is necessary to have low intrinsic noise, particularly at low frequencies, in the Earth's magnetic field ~ 50 μT. There are two cases of practical interest: (i) SQUIDs that are cooled and operated in an unshielded environment, and (ii) SQUIDs that are required to move through static fields. In both cases, the low frequency noise arises from the thermally activated hopping of flux vortices created in the devices during cooling or while moving. The uncorrelated hopping of these vortices produces a 1/f noise power spectrum.

Over recent years, we have studied the low frequency noise of HTS SQUIDs and of magnetometers both cooled in a static magnetic field, and after a change in applied magnetic field. In this chapter, I'll first discuss the narrow structure concept and then present data from bare SQUIDs, single layer magnetometers and multilayer magneto-meters cooled in a static magnetic field followed by data after a change in magnetic field.

3   Flux Vortices in Narrow Lines

The concept of the narrow linewidth structure is based on a private communication from Prof. J. R. Clem, whose use of Gaussian units I adopt in this section.

Let us consider a type-II superconducting strip of width w and thickness d, which is cooled in a perpendicular applied magnetic field B_a through its transition temperature T_c as shown in Fig. 4-1. When the strip is cooled just below T_c in the presence of the applied magnetic field, it is filled with a gas of vortex-antivortex pairs. At low temperatures, when all the antivortices annihilate with vortices, the applied magnetic field makes it energetically favorable to have an excess number of vortices pinned in the strip. The remaining vortex density is B_a/Φ_0 with a vortex spacing of approximately $(\Phi_0/B_a)^{1/2}$. If the applied magnetic field B_a is large enough for the vortex spacing to be smaller than the width of the strip w, namely, $B_a \gg \Phi_0/w^2$, many vortices will be left in the strip after it has cooled to its final temperature.

Consider a region of the film in which there is only one vortex. Since the freeze-out process occurs mainly when the two dimensional screening length $\Lambda = 2\lambda^2(T)/d$ is much larger than the film width w, the primary contribution to the energy of a vortex in a film is kinetic energy. In addition, screening effects, which occur on the scale of the 2D screening length, can be neglected. The self-energy of the vortex as given by Clem[40] is

$$U_s = \frac{\Phi_0^2}{8\pi^2\Lambda} \ln\left[\frac{2w}{\pi\xi} \sin\left(\frac{\pi x}{w}\right)\right] \tag{4-1}$$

for $\xi/2 < x < w-\xi/2$, where ξ is the coherence length. Note that the self-energy of the vortex is zero at the edges and reaches a maximum at the center of the strip, $x = w/2$.

In the presence of the perpendicular applied field B_a and under the condition $\Lambda > w$, the supercurrent induced in response to the applied field is

47
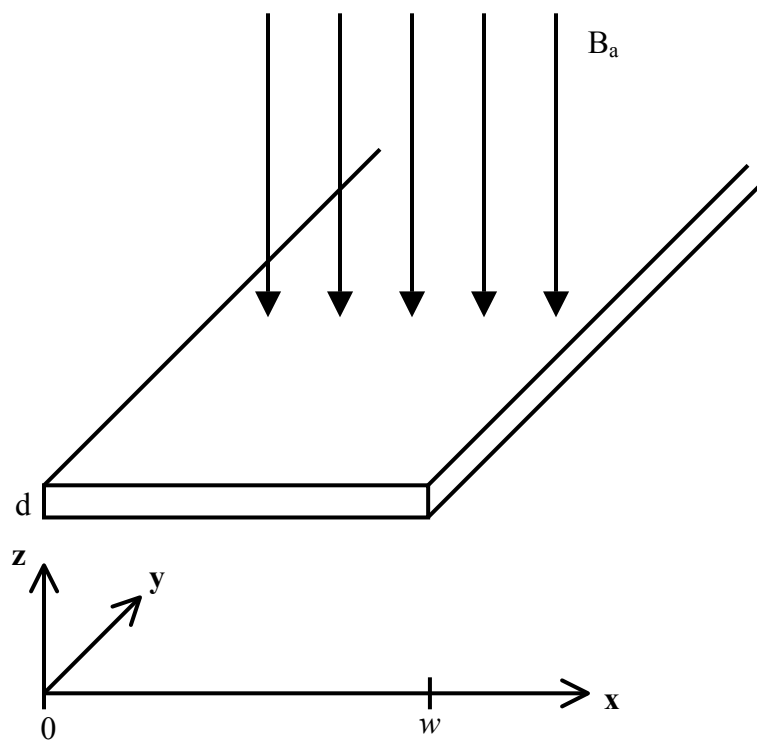
Fig. 4-1 Schematic view of a superconducting strip of width *w* in a perpendicular magnetic field.

$$J_{ay}(x) = -\frac{c\,B_a}{4\pi\lambda^2}(x - w/2). \tag{4-2}$$

This leads to a Lorentz force on the vortex

$$F_{ax}(x) = \frac{J_a\Phi_0 d}{c} = -\frac{\Phi_0 B_a}{2\pi\Lambda}(x - w/2). \tag{4-3}$$

The corresponding interaction energy is given by integrating Eq. 4-3:

$$U_a(x) = \frac{\Phi_0 B_a}{4\pi\Lambda}x(w - x). \tag{4-4}$$

Therefore, the total Gibbs free energy of a vortex at position x is

$$G(x) = U_s(x) + U_a(x) = \frac{\Phi_0^2}{8\pi^2\Lambda}\ln\left(\frac{2w}{\pi\xi}\sin\frac{\pi x}{w}\right) - \frac{\Phi_0 B_a}{4\pi\Lambda}x(w - x). \tag{4-5}$$

The minimum Gibbs free energy occurs when $x = w/2$,

$$G\left(\frac{w}{2}\right) = \frac{\Phi_0^2}{8\pi^2\Lambda}\ln\left[\left(\frac{2w}{\pi\xi}\right)\left(1 - \frac{B_a}{B_{c1}^*}\right)\right], \tag{4-6}$$

where

$$B_{c1}^* = \frac{2\,\Phi_0}{\pi\,w^2}\ln\left(2w/\pi\xi\right). \tag{4-7}$$

For $B_a > B_{c1}^*$, the Gibbs free energy becomes negative at $x = w/2$; therefore, a row of

vortices will be produced as the strip is cooled through T_c. However, if the applied field

is just below B_{c1}^*, the flux vortices will not be guaranteed to be expelled from the strip.

This is due to the local minimum of Gibbs free energy, shown in Fig. 4-2, for values of

B_a in the range $B_x < B_a < B_{c1}^*$, where
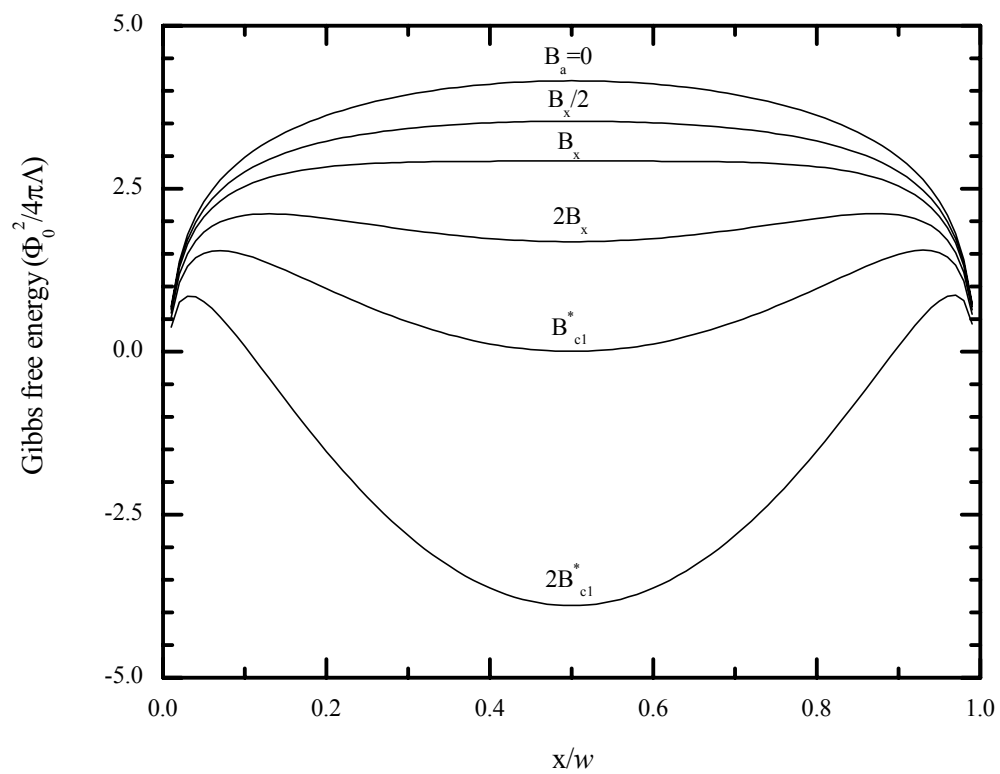
Fig. 4-2 Gibbs free energy of a vortex vs. its position x in a strip of width *w*.

$$B_x = \frac{\pi \Phi_0}{4w^2}. \tag{4-8}$$

For values of the applied field larger than B_x, there is a local minimum at the center of the strip with local maxima at both edges, $x = w/2 \pm \Delta x$. It is likely that near T_c a thermally activated vortex will find itself trapped in the local potential well. As the temperature decreases through T_c, the barrier height $\Delta G = G (x_{max}) - G (w/2)$ increases rapidly. The probability of the vortex escaping out of the well is proportional to $\exp(-\Delta G / k_B T)$. Thus it is highly unlikely for the vortex to escape. Therefore, to avoid flux vortices being trapped in the strip during cooling the applied magnetic field must be less than the threshold field B_x.

The threshold field is best seen from the expression for the net force

$$F_x (x) = -\frac{dG(x)}{dx} = \frac{\Phi_0^2}{8\pi\Lambda w} \tan\left[\frac{\pi}{w}\left(x - \frac{w}{2}\right)\right] - \frac{\Phi_0 B_a}{2\pi\pi}\left(x - \frac{w}{2}\right), \tag{4-9}$$

where $F_x (w/2) = 0$, with respect to the local minimum. The local maximum occurs at $x = w/2 \pm \Delta x$, thus

$$\frac{\tan\left(\pi\Delta x/w\right)}{\pi\Delta x/w} = \frac{B_a}{B_x}. \tag{4-10}$$

For $B_a < B_x$, there is only a single local maximum at $x = w/2$. Hence, the threshold field B_x defines the static magnetic field where the Gibbs free energy at the center of the strip changes from positive to negative, and thus creates possibilities of flux vortices being trapped in the strip. In other words, for a superconducting strip of width w

cooled in a perpendicular static magnetic field, the flux vortices will be expelled from the strip for fields less than its threshold value B_x.

However, when the superconducting strip is cooled in a magnetic field below the threshold and is then subjected to a change in magnetic field, a supercurrent will be induced. Above a threshold value, the induced supercurrent is sufficient to drive vortices into the strip. The threshold current to drive a vortex into a superconducting strip of width w can be found from[41]

$$ I_T = I_c \, d \, w \left[2.46 \left(\Phi_0 / w^2 H^* \right)^{1/4} \right], \tag{4-11} $$

where I_c is the critical current of the strip, d is the thickness of the strip, and H^* is a characteristic field defined by $H^* = 2\pi J_c d / c$. (In practical units $H^* = 6.28 \times 10^{-9} J_c d$, where H^* is in gauss, J_c in A/cm^2, and d in angstroms.) We see that I_T is proportional to $w^{3/2}$.

4.2   Measurement in Static Magnetic Fields

4.2.1 Experimental setup

In order to measure noise in SQUIDs cooled in a static magnetic field, we use the apparatus for measuring the noise in zero field. To eliminate the current fluctuation in magnetic field during the cooling, a 0.1m long HTS tube is placed around the SQUID inside the solenoid. The mu-metal can is removed to reduce the magnetic field distortion. The probe is lowered into liquid nitrogen with a current in the solenoid that is maintained

throughout the measurement. The entire assembly is placed inside a rf shielded room.

The circuit diagram of the current supply for external magnetic field is shown in Fig. 4-3.

The LM 317 voltage regulator is powered by three lead-acid batteries in series. The gate

resistor R_c defines the magnitude of current. The 100 Ω resister is used to measure the

current flowing into the solenoid. Since we don't have means to thermally cycle the HTS

tube, each measurement in a different field requires us to warm up the whole probe. As a

precaution against trapped flux induced by thermoelectric currents, the probe is cooled

very slowly from room temperature to 77 K.

4.2.2 Bare SQUIDs

As an illustration, noise spectra of a solid washer SQUID cooled in both zero field

and 63 μT are shown in Fig. 4-4. The spectra clearly shows that the 1/f noise increases

dramatically when the solid washer SQUID is cooled in 63 μT, which is only a little

above the earth's magnetic field $\sim$ 50 μT. Therefore, we patterned the SQUID washer

into narrow lines and repeated the measurement.

Two types of SQUIDs are discussed here: bicrystal SQUIDs (BC1 and BC2) and step

edge SNS SQUIDs (SNS1 and SNS2), shown in Fig. 4-5. In addition, two kinds of

design are used: with junctions outside the washer (BC1) and junctions inside the washer

(BC2, SNS1 and SNS2). No matter what types of junction or design, we keep the outer

dimensions of the SQUIDs identical, 488 μm $\times$ 492 μm. Furthermore, each SQUID
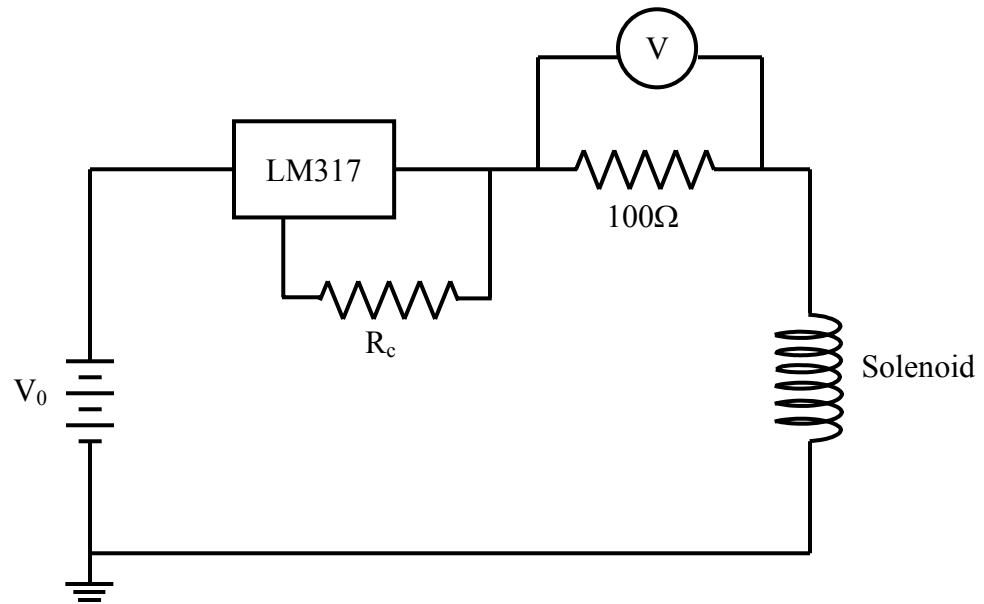
Fig. 4-3 Circuit diagram of the static current supply.
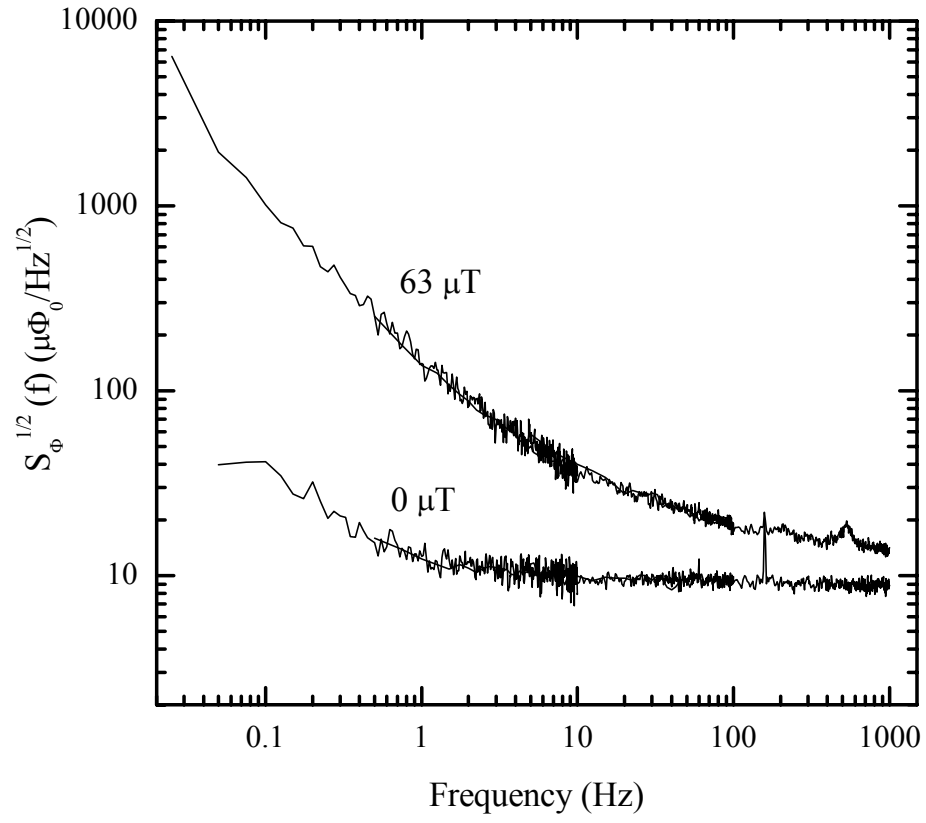
Fig. 4-4 Flux noise spectra $S_\Phi^{1/2}(f)$ of the solid washer SQUID cooled in zero field and in 63 μT.

(a) 200 μm

(b) 100 μm

(c) 200 μm

(d) 100 μm

(e) 100 μm
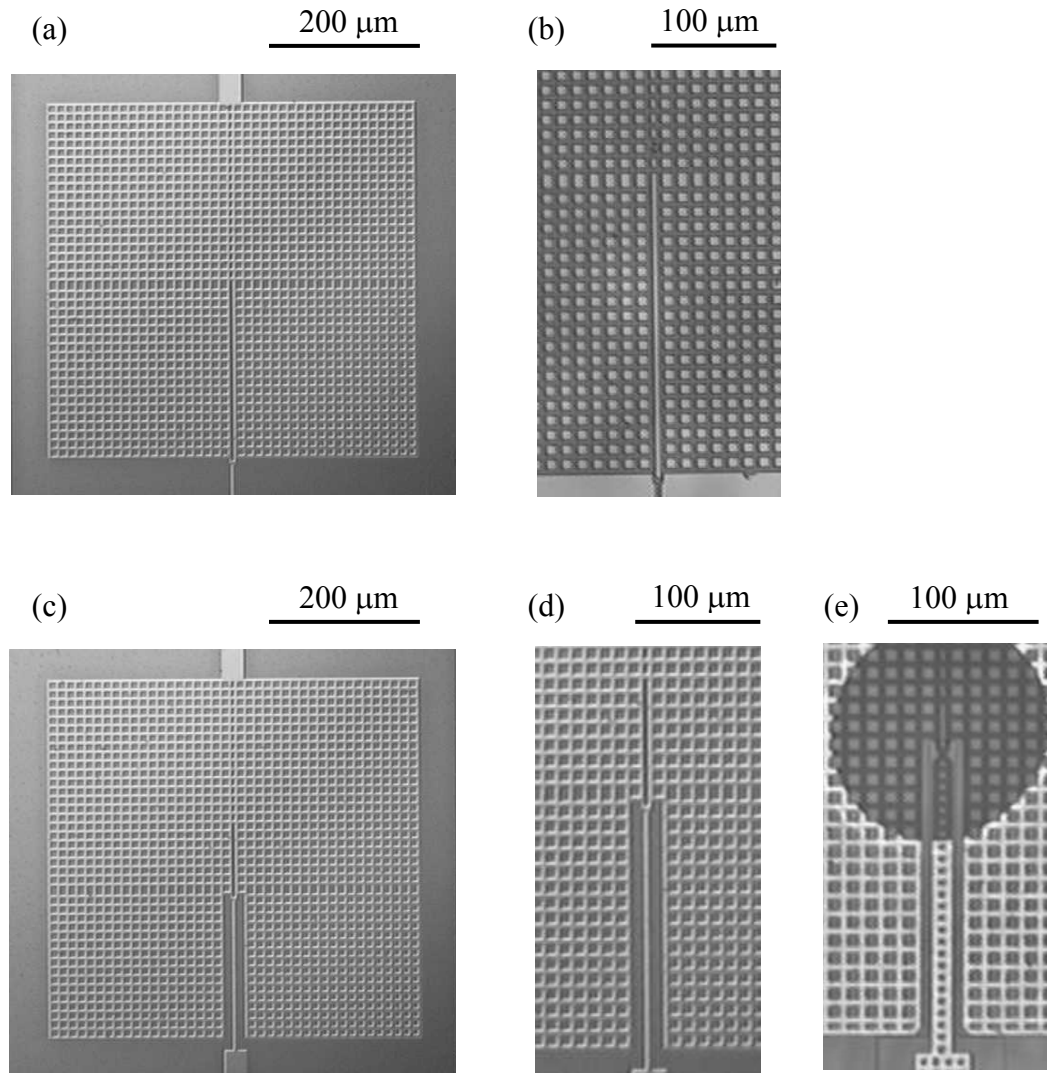
Fig. 4-5 Photographs of the photomasks for (a) SQUID with junctions outside the washer (BC1) and (c) SQUID with junctions inside the washer (BC2); the higher magnification photographs of (b) SQUID BC1, (d) SQUID BC2, and (e) SQUID SNS1.

washer is patterned so that no portion of the $YBa_2Cu_3O_{7-\delta}$ film is wider than 4 μm. For bicrystal SQUIDs, we patterned the washer into grids with 4 μm-wide $YBa_2Cu_3O_{7-\delta}$ film and 8 μm × 8 μm holes. The estimated inductances of bicrystal SQUIDs are 100 pH for junctions outside the washer, such as BC1, and 50 pH for junctions inside the washer, such as BC2. The inductances of step edge SQUIDs tend to be smaller due to the shorter lengths of the SQUID slits compared with those of bicrystal SQUIDs.

Each SQUID in turn is mounted on the noise probe, and its noise is measured after it is cooled in a static field. In each static field, we took at least six noise spectra in two thermal cyclings. The flux noise spectra of the bicrystal SQUID BC1 and the step-edge SQUID SNS1 cooled in static fields are shown in Fig. 4-6 (a) and (b), respectively. The 1/f noise of BC1 remains the same for fields up to 90 μT and increases dramatically in fields above 100μT. However, the 1/f noise of SNS1 increases gradually in cooling fields below 100 μT. We noticed that the bias current of SNS1 decreases as the applied field increases. We now plot the field noise at 1 Hz versus cooling field for both BC1 and BC2, and SNS1, shown in Fig. 4-7 (a) and (b). In Fig. 4-7 (a) the open square indicates the noise taken from BC1, down triangles from BC2, and stars from the solid washer SQUID. The noise at 1Hz for both BC1 and BC2 does not change for fields up to 100 μT, which is in good agreement with Clem's prediction. At 60 μT the noise at 1 Hz for the solid washer SQUID is one order of magnitude higher than that of SQUIDs with narrow lines. Note that at a cooling field 115 μT the noise at 1 Hz does not increase as we expect. To be sure of this result, we have repeated the measurement on both bicrystal
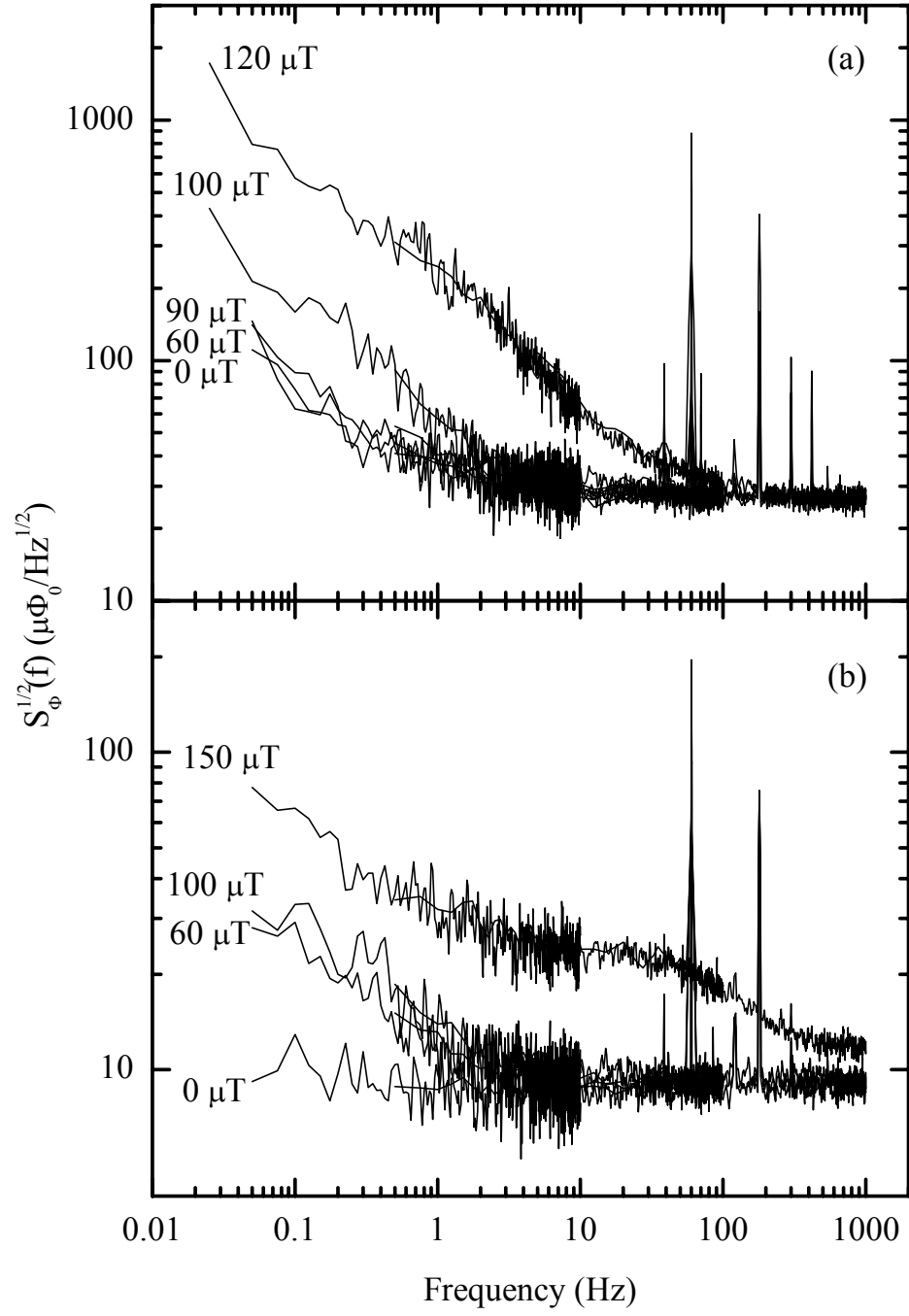
Fig. 4-6 Flux noise spectrum of (a) bicrystal SQUID BC1 and (b) step edge SQUID SNS1 cooled in different static fields.
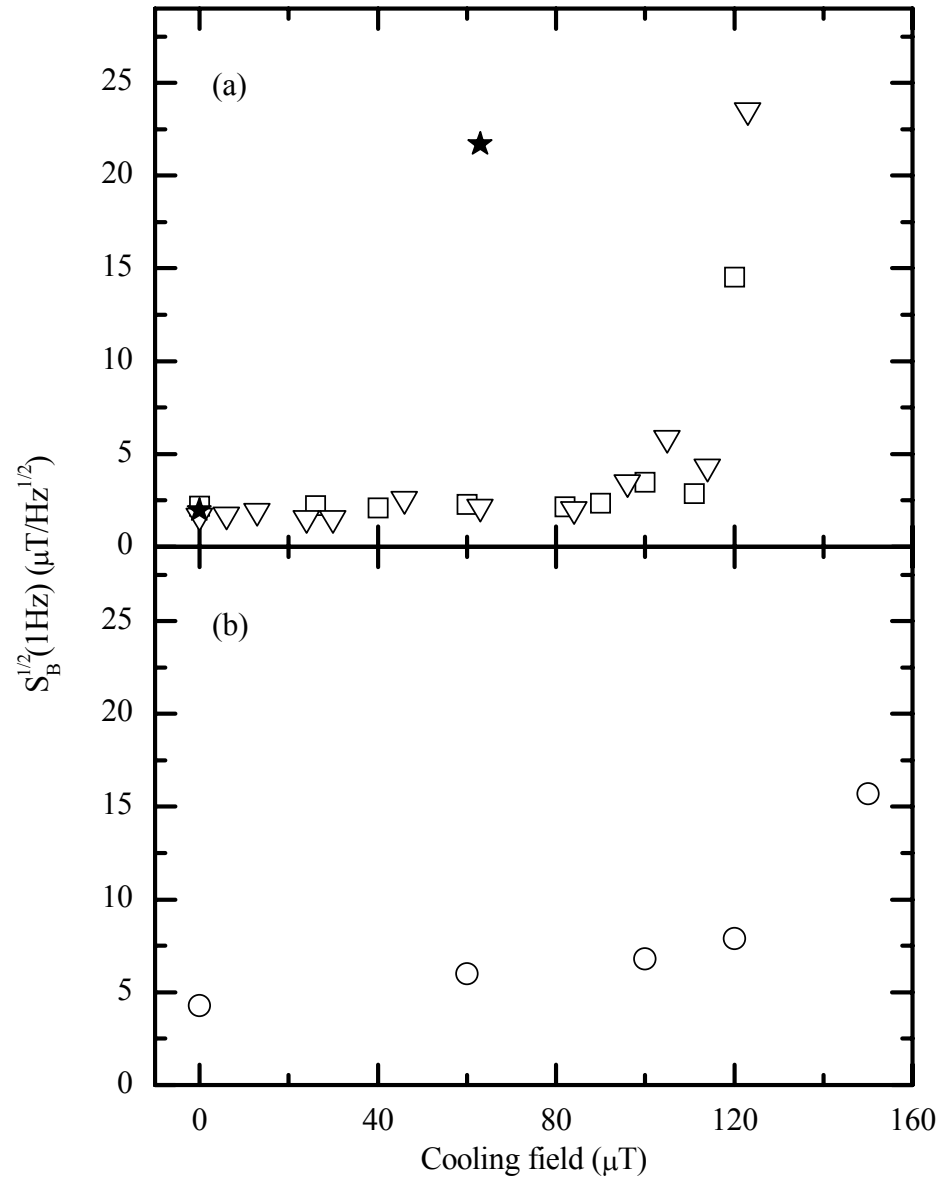
Fig. 4-7 Field noise at 1 Hz in different cooling fields for (a) bicrystal SQUIDs
(BC1-open squares, BC2-open down-triangles and the solid washer-stars), and (b)
step edge SQUID SNS1 (open circles).

SQUIDs several times in several different cool down. This "dip" has puzzled us for quite a long time. It turns out to be the filling effect[42] –there are integer numbers of flux vortices hold by supercurrent in each hole, which forms a stable state. In this case, $115\mu T$ corresponds to eight flux vortices contained in each hole. However, we did not observe the same effect in step edge SQUID SNS1.

Another interesting result we found is that the effective area of SQUIDs with narrow lines is larger than that with the solid washer even though the designs of the SQUIDs are the same. Namely, the outer dimensions of the SQUID washer and the length of the SQUID slit are the same for SQUIDs with narrow lines and with solid washer. For example, for the bicrystal SQUIDs which have junctions outside the washer the effective area is 0.033 mm^2 for SQUIDs with narrow lines (BC1) and 0.029 mm^2 for the solid washer SQUID. The same result is found for the effective area of SQUIDs with junctions inside the washer, that is, an increase of 10% for the SQUID washer with narrow lines compared with the solid washer SQUID.

4.2.3 Directly Coupled Magnetometers

Since the effective area of bare SQUIDs is rather small, we commonly use the directly coupled magnetometer[43,44] which requires only a single layer $YBa_2Cu_3O_{7-\delta}$ process; the effective area of a carefully designed directly coupled magnetometer can be 10 times larger than a bare SQUID. A directly coupled magnetometer consists of a SQUID connected in parallel with a large-area pickup loop. While noise due to vortex

motion in the SQUID itself can be eliminated by using a narrow-lines SQUID washer, it is possible that the pickup loop gives rise to excess 1/f noise in the device. The motion of vortices in the pickup loop might couple flux to the SQUID in two ways: the vortex motion can directly couple flux to the SQUID, by causing the field lines to move into or out of the SQUID, and vortex motion in the pickup loop can couple flux indirectly to the SQUID by means of the screening supercurrent. To minimize the flux directly coupled to the SQUID, we design the magnetometers to keep the SQUID sufficiently far (100 μm) from any wide films of the pickup loop.

For indirect flux noise, calculations by Ferrari *et al.*[45] indicate that the 1/f noise of the pickup loop is negligible for any reasonable magnetometer configuration. To investigate the noise of single layer magnetometers cooled in magnetic fields, we made three magnetometers (MAG1, MAG2, and MAG3), and measured their noise in different cooling fields. Figure 4-8 shows the configuration of the directly coupled magnetometer, with an enlarged drawing of the SQUID area in Fig. 4-8 (b). The typical magnetometer used at UC-Berkeley consists of a 4 μm-wide SQUID body connected to the pickup loop (with outer and inner dimensions of 100 mm and 20mm, respectively) which is 120μm away from the SQUID body. However, we found that each device exhibits an abrupt increase in 1/f noise when the cooling field is increased from zero to a few microtesla, after which the noise is more or less unchanged in cooling fields up to about 100 μT. The field noise of magnetometers at 1 Hz in different cooling fields is plotted in Fig. 4-9. After 100 μT, the field noise at 1Hz increases again as flux begins to penetrate the 4 μm washer of the SQUID. We ultimately found that this unusual dependence on field arose

(a)

10 mm

(b)

48 μm

grain
boundary
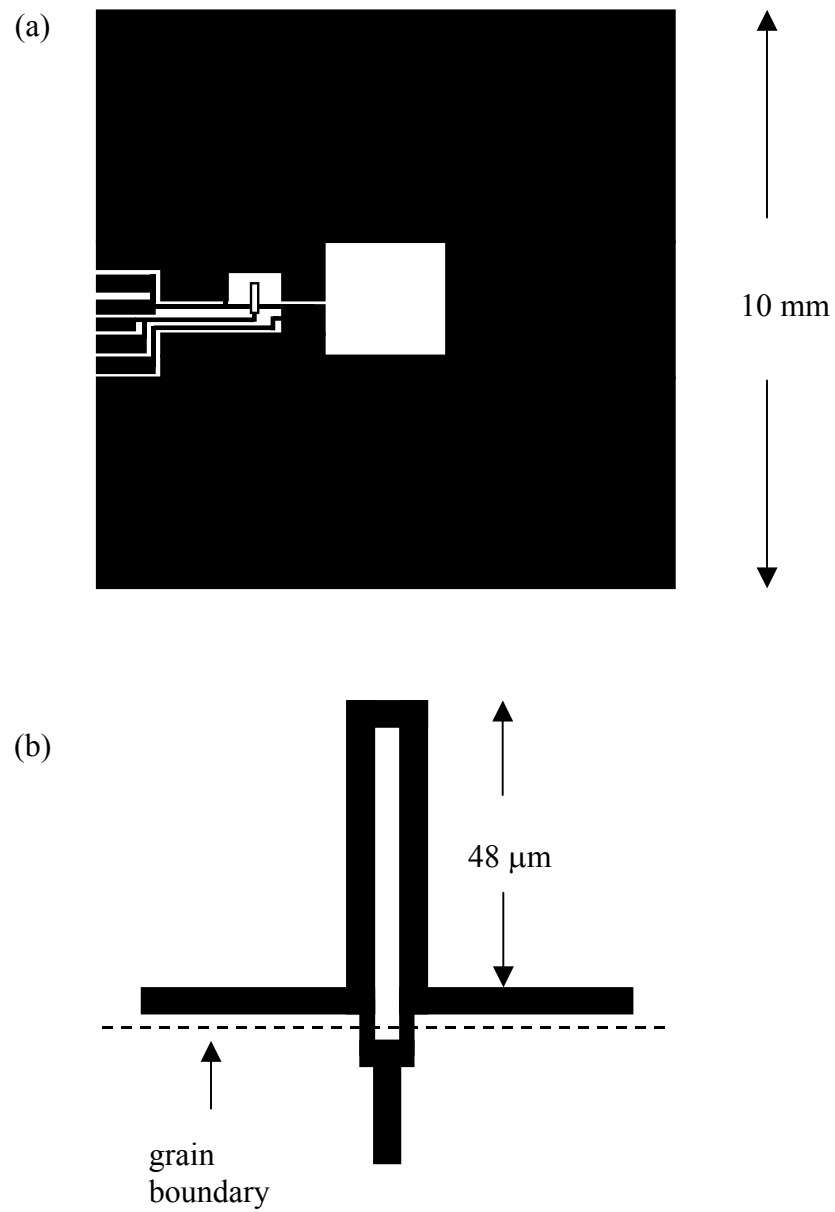
Fig. 4-8 (a) Schematic drawing of a typical magnetometer (not to scale); (b) an
enlarged drawing around the SQUID body.
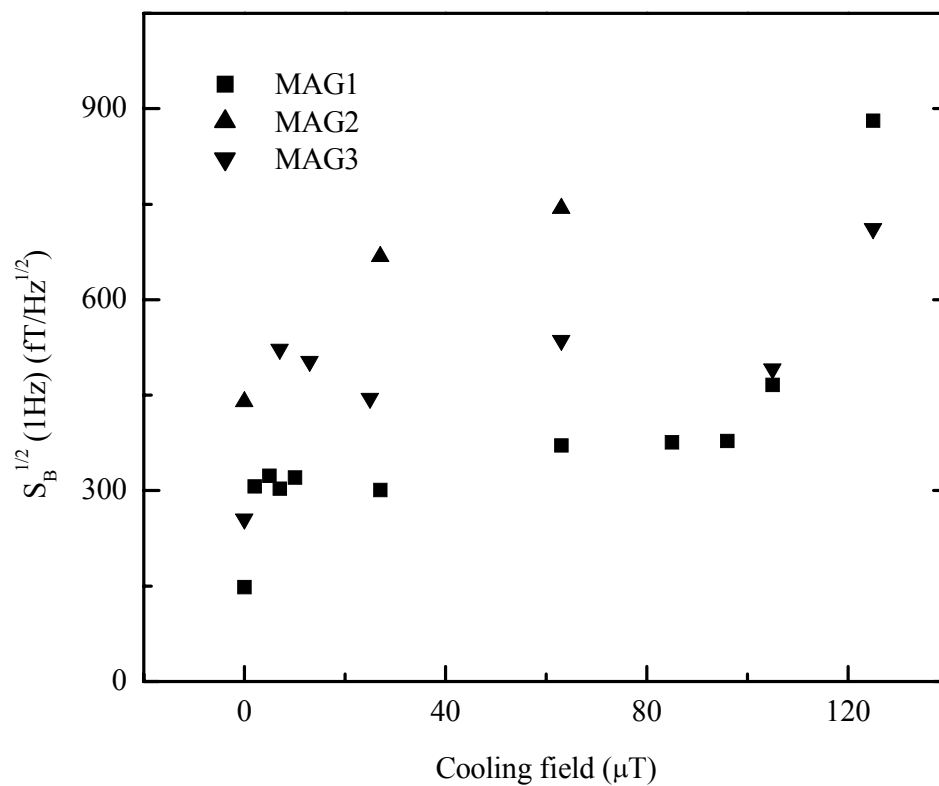
Fig. 4-9 The field noise of three magnetometers with solid pickup loops at 1 Hz in different cooling fields: MAG1-squares, MAG2-uptriangles, and MCG3-down-triangles.

63
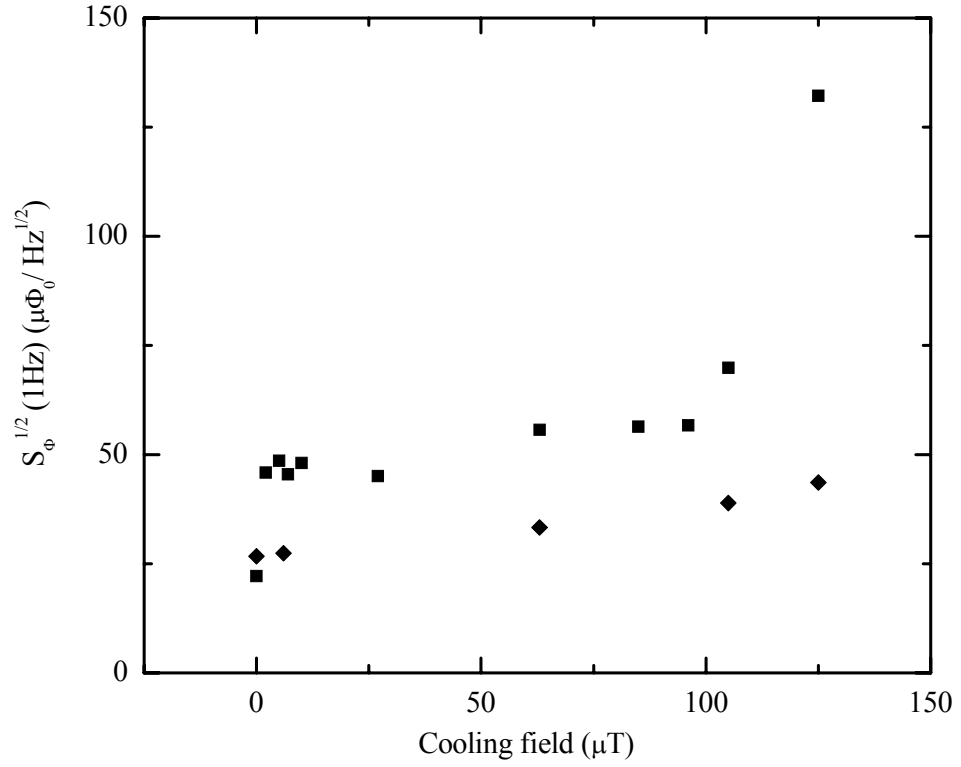
Fig. 4-10   Fields noise of MAG1 at 1 Hz in different cooling fields before (squares) and after (rhombuses) re-patterning to remove the tapered edges of the pickup loop.

from the tapered outer edges of the magnetometer pickup loop. Therefore, we re-patterned MAG1, removing the thinner YBCO film where the substrate had been held in a clip to leave a sharp edge. The outer dimension of the pickup loop was reduced from 8-8.5 mm to 7.3 mm. The results are plotted in Fig. 4-10. The tapered outer edges were an artifact of the deposition process. The fact that the noise of the device, which was re-patterned once, is flat to around 100 μT indicates that vortex motion in the pickup loop no longer contributes to the intrinsic low-frequency noise of the device. We conclude that the abrupt increase in noise in fields below 100 μT was due to a large number of traps in the tapered region with low pinning energies and low barriers to flux entry that become saturated at very low applied fields.

To study the effect of the narrow lines in directly coupled magnetometer further[46], we made two more magnetometers with narrow linewidths. The first of these devices (MAG-N1) has a pickup area consisting of two loops delineating the inner and the outer edges of its washer. The inner and outer dimensions are 2 mm and 8 mm, respectively. Each of these loops involves a network of 4 μm lines. The second device was made by re-patterning solid pickup loop magnetometer MAG3. We re-patterned MAG3 in two steps: first, we patterned the area of 10 mm × 10 mm around the SQUID body to narrow lines, MAG3-R1; secondly, we patterned the entire pickup loop into narrow linewidths, MAG3-R2. Figure 4-11 shows the configuration of both devices. The noise of MAG-N1 and MAG3-R2 in different cooling fields, shown in Fig. 4-12, remains relatively flat in fields up to 100 μT, which it what we expect.

(a)

100 μm

(b)

(c)

500 μm
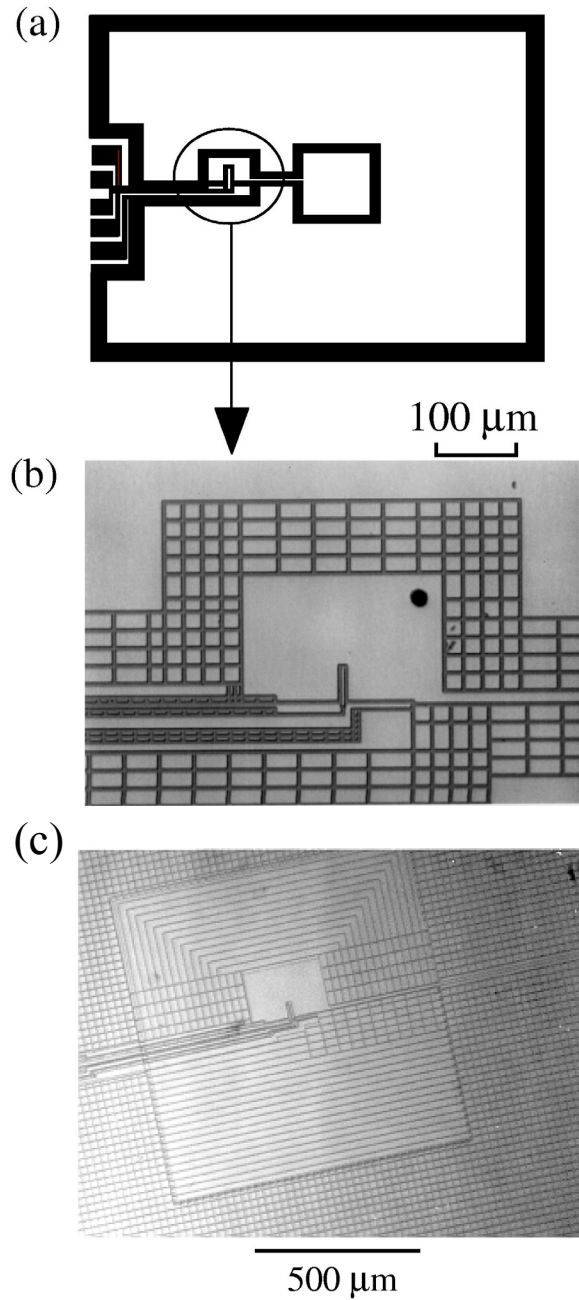
Fig. 4-11 (a) Configuration of narrow linewidth magnetometer MAG-N1. The SQUID body is enlarged for clarity. (b) Optical photograph of the area surrounding the SQUID. (c) Optical photograph of portion of MAG3-R2 after re-patterning twice. The square area near the SQUID body was first patterned and the rest of pickup loop was patterned in second process.
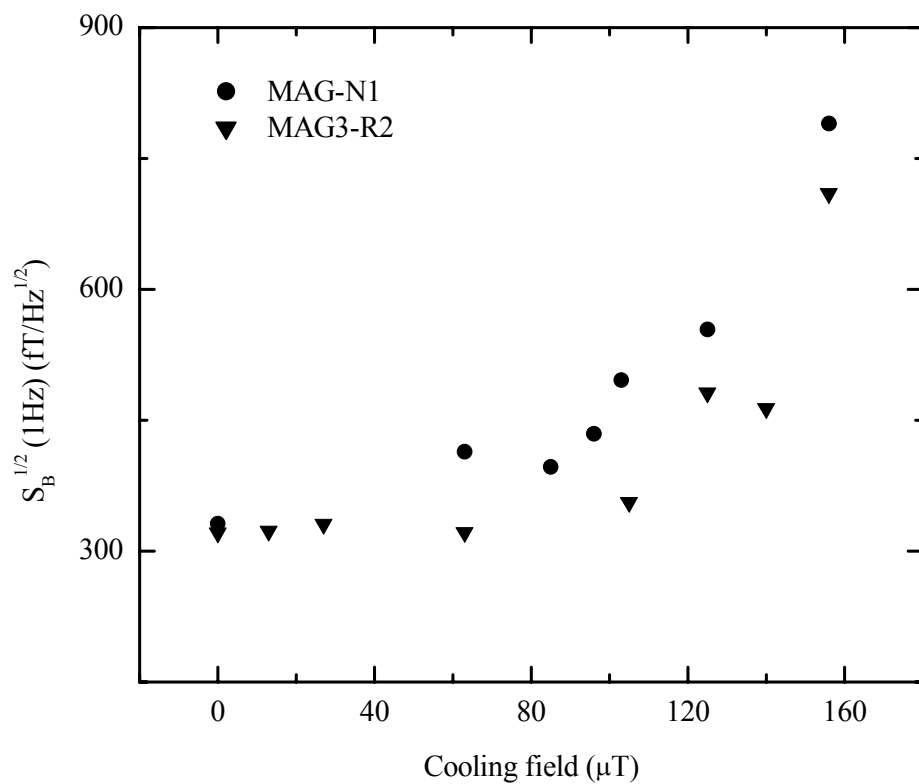
Fig. 4-12 Field noise at 1 Hz in different cooling fields for two narrow linewidth magnetometers: MAG-N1 (circles) and MAG3-R2 (down-triangles).

However, the effective area varies substantially. For all the solid washer magnetometers, the effective area is 0.28-0.29 mm^2. For MAG-N1, the effective area is only 0.14 mm^2, approximately a factor of 2 lower than that of a solid-washer magnetometer of the same dimension. An interesting result was observed on the re-patterned magnetometers MAG3-R1 and MAG3-R2. The effective area of MAG3-R1, which was patterned in an area of 10 mm × 10 mm around the SQUID body to narrow lines, is 0.33 mm^2, a 15 percent increase over solid washer devices. The effective area of MAG3-R2, whose pickup loop was patterned into a mesh of 4 μm lines, is 0.3 mm^2, only a slight increase over solid washer magnetometers.

4.2.4 Multilayer Magnetometers

Another way to increase the effective area of the device is to fabricate multilayer magnetometers[47,48]. In fact the lowest levels of magnetic field noise at frequencies above the 1/f noise are obtained with a flux transformer involving a multilayer, multiturn coil that is inductively coupled to a dc SQUID. In our collaboration with MagneSensors Inc., they made multilayer, multiturn flux transformers for us. Thus, we could study the noise of such multilayer devices cooled in static fields.

Two types of $YBa_2Cu_3O_{7-\delta}$ -$SrTiO_3$-$YBa_2Cu_3O_{7-\delta}$ multilayer flux transformers were made: one without flux dams[49,50] and the other with flux dams in each of the four parallel pickup loops (Fig. 4-13 (c)). Each multilayer flux transformer (Fig. 4-13 (a))

(a)   10 mm

(b)   200 μm

(c)   200 μm

(c)
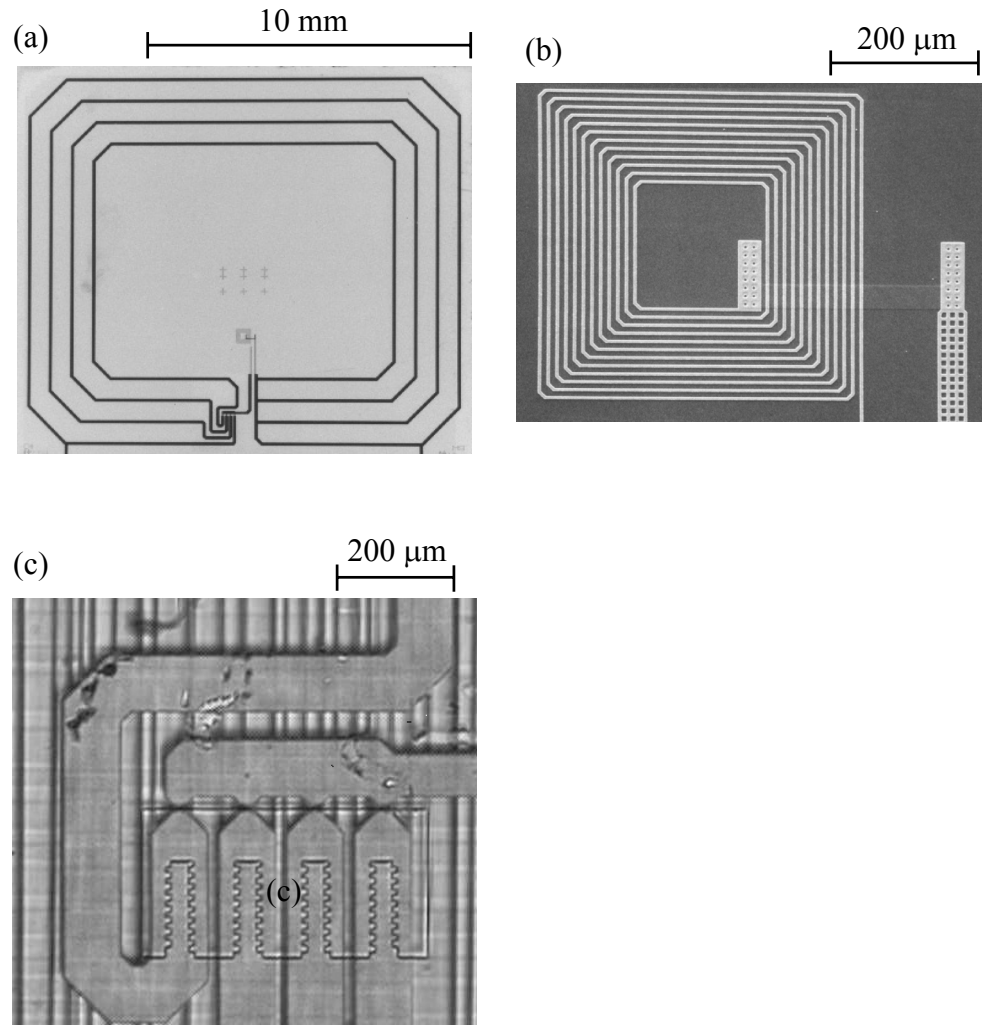
Fig. 4-13   Scanning electron micrographs of (a) flux transformer, (b) multiturn input coil and (c) flux dams.

consists of four parallel pickup loops with outer dimensions 10 mm × 12 mm, connected to an input coil of 12 turns, each 4 μm wide (Fig. 4-13 (b)). The crossover, connecting the innermost turn of the input coil to the pickup loop, is 34 μm wide. Each SQUID in turn was inductively coupled to the input coil of a transformer in a flip-chip arrangement.

Figure 4-14 shows the flux noise at 1 Hz in different cooling fields. For bicrystal SQUID BC2 coupled to the transformer without flux dams (FT), the noise is unchanged for cooling fields up to 68 μT, and increases slightly for cooling fields up to 100 μT and dramatically at fields above 120 μT. For step edge SQUID SNS2 coupled to the transformer with flux dams (FT/FD), the 1/f noise increases gradually for cooling fields up to 80 μT, and steeply at fields after 120 μT. In both case, the threshold field is lower in the presence of the flux transformer than for the bare SQUID. It is possible that the lower threshold field is due to flux entry to the crossover, which is 34 μm wide. Another possibility is that random alignment of the turns of the input coil and the holes in the SQUID washer produces regions that are effectively more than 4 μm wide. Nevertheless, both multilayer magnetometers exhibit no increase in 1/f noise in a cooling field of 50 μT. In addition, the flux transformers with or without flux dams do not show any difference for cooling in a static magnetic field.

As we realized for the effective area of a bare SQUID, the effective area is larger if the SQUID washer is full of holes. We also flip-chipped solid washer SQUIDs to the flux transformers. Predictably, the effective area of the magnetometer involving a

70
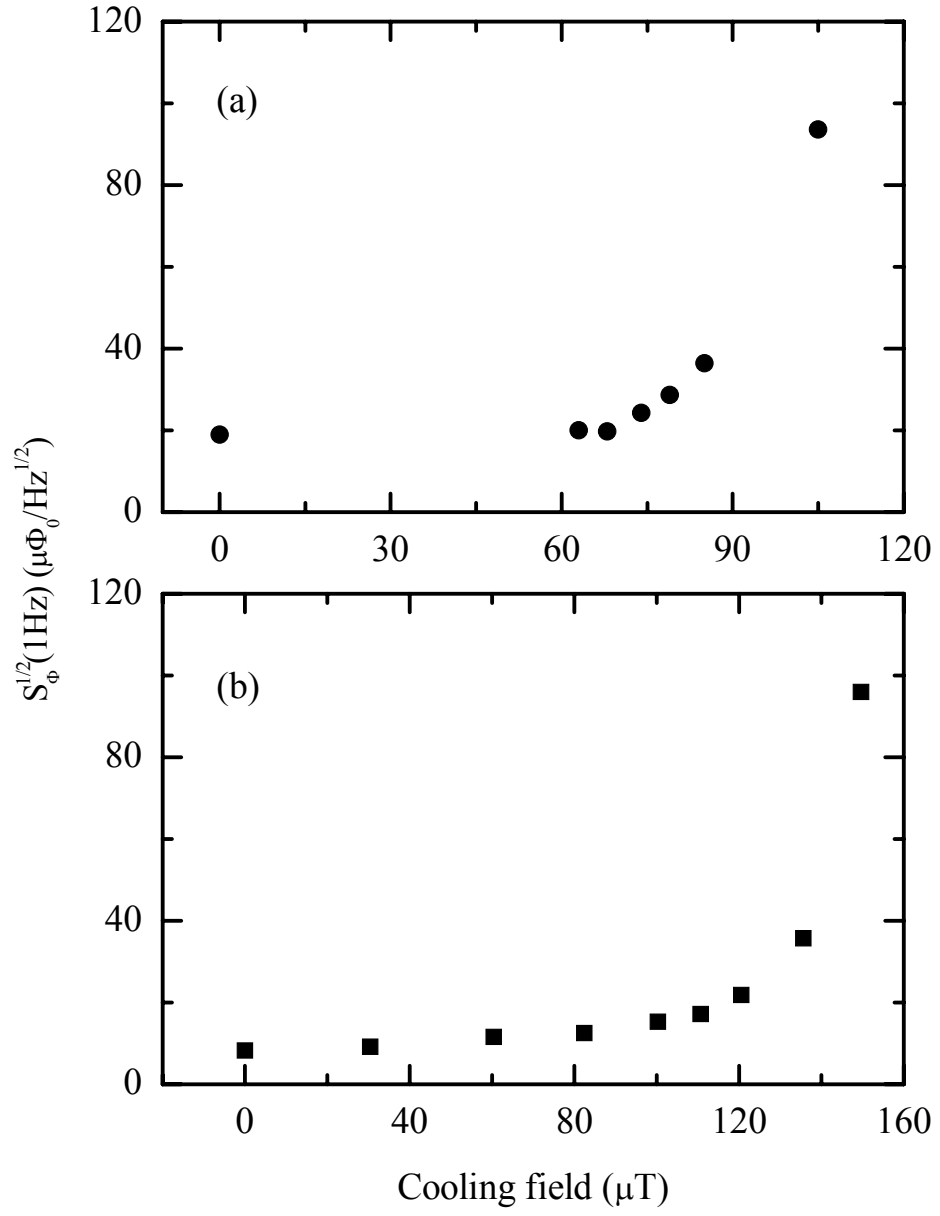
Fig. 4-14 Flux noise of magnetometers at 1 Hz in different cooling fields: (a) BC1+FT, and (b) SNS2+FT/FD.

SQUID with narrow lines coupled to a transformer is about 20% larger than that of the magnetometer consisting of a solid washer SQUID coupled to the transformer. As an example, the effective area of BC2+FT is 0.876 mm^2, an increase of about 20 percent over the 0.712 mm^2 effective area of a solid washer SQUID (same design as BC2)+FT.

4.3 Measurement in a Change in Magnetic Fields

4.3.1 Setup

In order to apply a uniform magnetic field which is subsequently turned off, we removed the HTS tube, and varied the solenoid current. The power supply circuit is shown in Fig. 4-15. A potentiometer is installed to vary the current. To prevent current drift from the batteries, we also use a switch to open the circuit open when the current is turned off to zero. The resistor R_M is used to regulate the maximum current and R_i to vary the current from its initial value to a non-zero current. Since the HTS tube is removed, we need only to thermally cycle the devices using the heater under them.

4.3.2 Bare SQUIDs

As a first attempt, we measured the noise in bicrystal SQUID BC1 after the following changes[51]: field switched on from zero, field turned off to zero, field switched on to a final value of 51 μT, and field turned off from an initial value of 51 μT. The results are shown in Fig. 4-16(a). Regardless of whether the device was cooled in zero
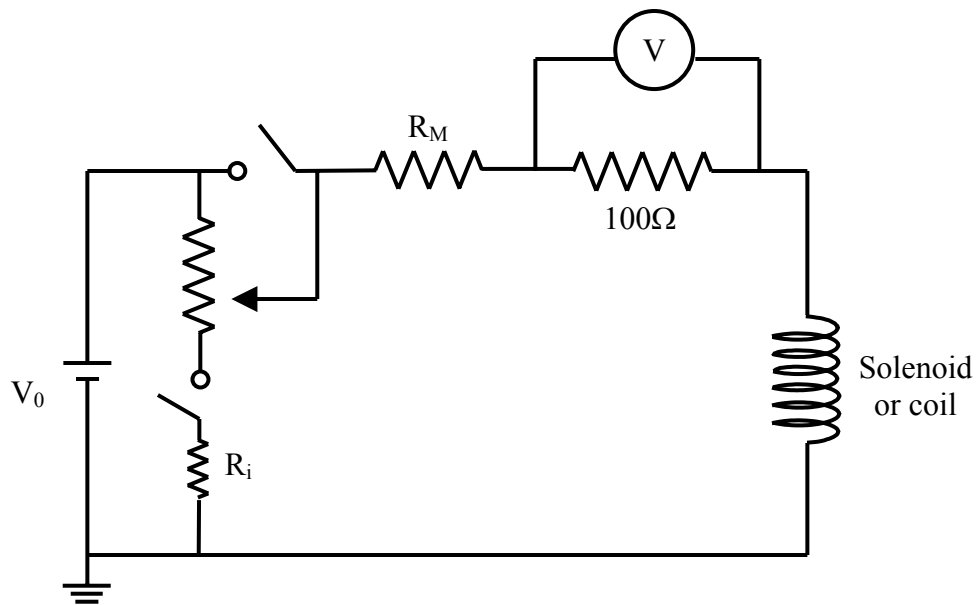
Fig. 4-15　Circuit diagram of current supply which can vary the current by a potentiometer.
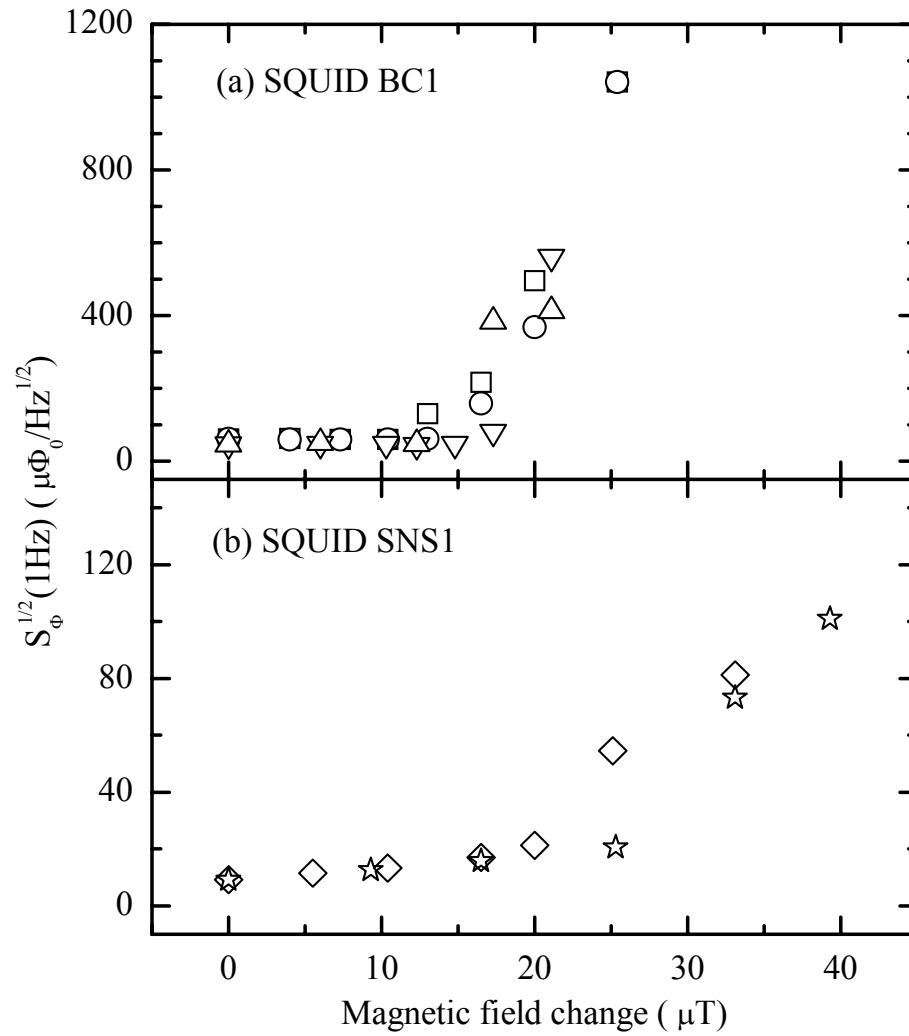
Fig. 4-16 Flux noise of SQUIDs at 1 Hz measured after a change in magnetic field. (a) four sets measurements in bicrystal SQUID BC1: magnetic field switched off to zero (squares), magnetic field switched on from zero (circles), magnetic field turned down from 51 μT (down-triangles), magnetic field turned up to 51 μT (up-triangles); (b) two sets measurements in step edge SQUID SNS1: magnetic field switched on from zero (rhombuses), magnetic field switched off to zero (stars).

field or a nonzero field, the data for each measurement set follow the same trend. The threshold applied field above which the noise increases is about 12 μT. On the other hand, for SNS1 with a smaller effective area, the threshold applied field is somewhat higher, about 25 μT [Fig. 4-16 (b)]. These results are consistent with a picture in which, above the threshold value, the flux vortices are driven into the 4 μm wide film by the induced supercurrent. The magnitude of the supercurrent is determined by the change in magnetic field, not by the initial cooling field. Thus for a given device we expect the low frequency noise to increase by the same amount for a given value of magnetic field change.

We also measured the noise of bicrystal SQUID BC2, which has junctions inside the washer and the grain boundary across the washer. However, no matter how small the change in magnetic field, BC2 exhibits random telegraph noise. We suspect that the grain boundary creates low energy pinning traps. Thus, the induced supercurrent will produce a Lorentz force on the flux vortices.

4.3.3 Multilayer Magnetometers

To extend the measurement to the multilayer magnetometer, it is necessary to restore the HTS tube around the magnetometer to reduce external magnetic field fluctuations. Changes in magnetic field are produced by a coil inside the tube. Because the 1/f magnetic field noise generated by the current in the coil was higher than that of

the magnetometers, we confined our measurements to turning off the applied field when the magnetometers were in the superconducting state.

For the flux transformer without flux dams (FT), the flux noise increases rapidly for very small field changes $\leq 2\ \mu T$. Thus, we report no further measurement on the flux transformer without flux dams.

The flux noise vs. the magnitude of the field switched off is plotted in Fig. 4-17. In Fig. 4-17 (a), data for BC1+FT/FD are compared with BC1, and in Fig. 4-18 (b) data for SNS1+FT/FD are compared with SNS1. For BC1, the presence of the flux transformer increases the field sensitivity by a factor of 43, while decreasing the threshold field to about $5\ \mu T$. For SNS1, the magnetic field sensitivity is increased by a factor of 32. There seems to be a reduction in the threshold field, but the scatter in the data makes this less well defined. Hence, the presence of the flux transformer with flux dams enhances the magnetic field sensitivity by a large factor while reducing the threshold field for 1/f noise increase by a much smaller factor.

We can interpret the reduction in threshold field of bare SQUID, B_T, in terms of the magnetic field applied to the SQUID by the supercurrent flowing in the flux transformer when the flux dam opens. In a separate experiment, we observed the magnetic flux coupled to the SQUID as the applied field was steadily increased. For fields above $B_{FD} \approx 0.16\ \mu T$, the flux in the SQUID no longer changed. Here, B_{FD} is the field at which the supercurrent induced in the flux transformer exceeds the critical current

76
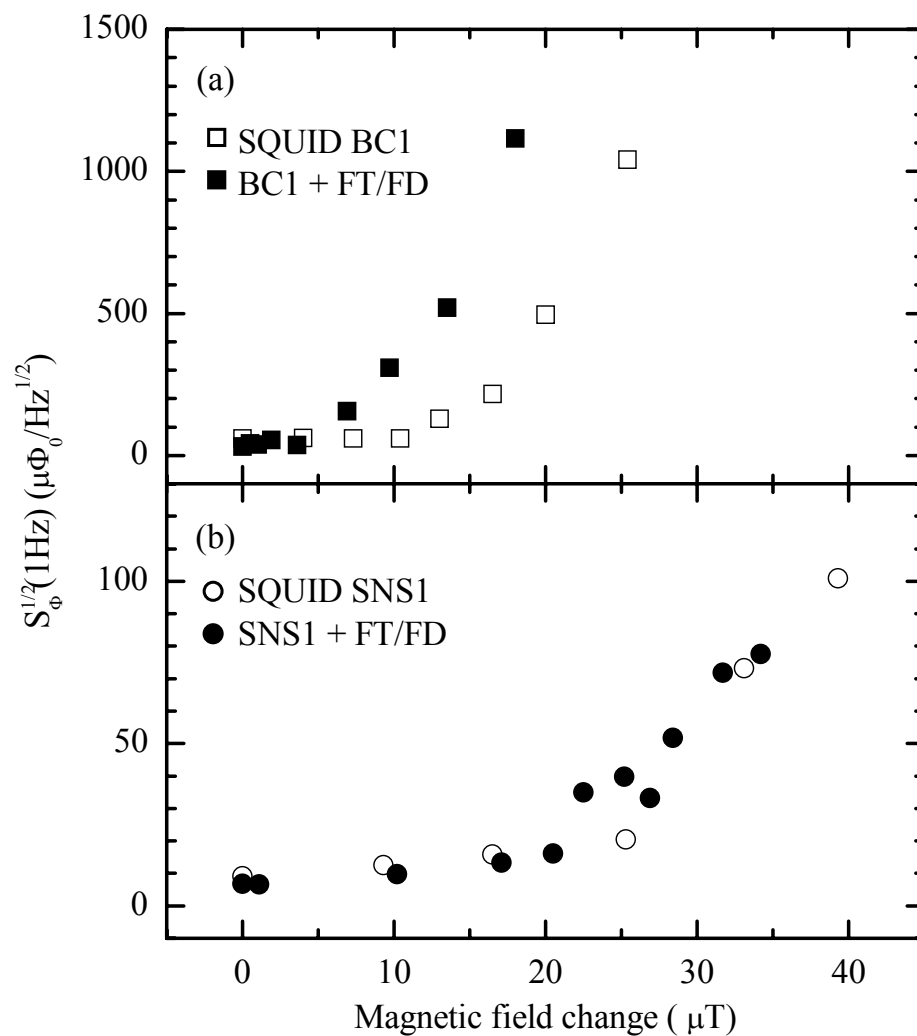
Fig. 4-17 Flux noise of SQUIDs at 1 Hz measured after magnetic field was turned off to zero. (a) Bare SQUID BC1 (open squares) and SQUID BC1+FT/FD (squares); (b) step edge SQUID SNS1 (open circles) and SQUID SNS1+FT/FD (circles).

of one of the flux dams, which thus switches to the open state. Since the flux transformer was designed so that flux coupled to the SQUID from the input coil is in the same direction as flux in the SQUID due to the change in magnetic field, we can show that the threshold field of the magnetometer is given by $B_T^m \approx B_T - B_{FD}(A_{eff}^m / A_{eff})$. Here, A_{eff} is the effective area of the bare SQUID and A_{eff}^m is the effective area of the multilayer magnetometer. Using the measured data, we found that the threshold field of the multilayer magnetometer of BC1+FT/FD is about 5 μT which is in good agreement with the data in Fig. 4-17(a). Because of the scatter in the data, we draw no conclusion for SNS1+FT/FD.

4.4   Discussion

In field-cooled experiments, bare SQUIDs with 4μm linewidths can be operated in cooling fields up to 100 μT with no increase in 1/f noise. In addition, the effective area of the SQUID with narrow lines is larger than that for solid washer SQUIDs. However, we do not observe any significant improvement in noise when narrow lines are employed in the pickup loops of directly coupled magnetometers, which consist of a SQUID body with 4 μm line width and the pickup loop is sufficiently far away from the SQUID. The effective area of the magnetometer with narrow lines, on the other hand, is larger than the magnetometer with a solid pickup loop. In the case of multilayer magnetometers, the addition of a flux transformer with or without flux dams enhances the magnetic field sensitivity by a large factor while somewhat reducing the threshold

78

cooling field above which the low frequency noise rises. We believe the wide crossunder and possibly the random arrangement of the input coil over the SQUID washer result in the lower threshold field. Nevertheless, the threshold value is still well above the earth's magnetic field.

When a magnetic field is applied to a bare SQUID, there is a threshold field above which the 1/f noise rises. Because the threshold field of a given device depends on the change in magnetic field, for a given device we expect the onset of low frequency noise to occur at a fixed value of field change. The presence of the flux transformer without flux dams substantially lowers the threshold field, whereas the flux transformer containing flux dams moderately lowers the threshold field. Thus in field change experiments, it is always the entry of flux into the SQUID that limits the performance of the magnetometer. The lowest threshold field, 5 μT for BC1+FT/FD, corresponds to a rotation of about $6^{\rm o}$ if the device is initially parallel to the earth's magnetic field and of about $25^{\rm o}$ if the device is initially perpendicular to the earth's field.

However, if we were to change the sense of the input coil, the threshold field would presumably be increased. The current flux transformer is wound so as to obtain the maximum sensitivity to magnetic field, thus lowering the threshold field. If the direction of the input coil were to be reversed, the effective area of the magnetometer would be reduced slightly, to a value $A_{\rm eff}^{\rm m}(1-2A_{\rm eff}/A_{\rm eff}^{\rm m})$. Nevertheless, the value of the threshold field would presumably have been increased to $B_{\rm T}+B_{\rm FD}(A_{\rm eff}^{\rm m}/A_{\rm eff})$,

according to our naive model. As an example, for BC1+FT/FD, the effective area would be reduced by 5% but the threshold field of the magnetometer would be increased to 19 µT. Thus, for experiments in which the magnetometer is required to move or rotate in the ambient field, the effect of reversing the sense of the input coil of the flux transformer should be considered.

Chapter V

Magnetocardiography in Ambient Magnetic Fields

Because of its high sensitivity to magnetic flux and magnetic field, a major application of SQUIDs is the detection of biomagnetic fields[52,53]—magnetic signals from the human brain—magnetoencephalography (MEG) —or heart—magnetocardiography (MCG). In these measurements, weak magnetic fields from localized sources are detected in the presence of background noise which is many orders of magnitude higher than the signal of interest. In ambient environments, the dominant sources of noise are the earth's magnetic field and 60 Hz signal and its harmonics from power lines. Some electrical instruments such as computers, elevators and automobiles also generate magnetic noise. In addition, radio frequency (rf) interference is also an issue; fortunately this source can be excluded by a thin layer of copper mesh surrounding the system. In order to reduce background noise, one uses a magnetically shielded room (MSR) or spatial gradiometers or often both. However, even MSRs[54] do not reduce the 60 Hz signal sufficiently. In fact, MRSs often produce low frequency noise gradients. Therefore, spatial gradiometers are required to discriminate strongly against external noise sources in favor of locally generated signals.

For decades, low-Tc first-derivative gradiometers have been highly developed and are used commercially in a variety of biomagnetic applications[55-57]. The gradiometer is made of two loops of niobium wire[58] or planar thin film loops[59] wound in opposition.

The former measures the axial gradient $\partial Bz/\partial z$ while the latter measures an off-diagonal gradient such as $\partial Bx/\partial z$. The axial first-derivative gradiometer, as an example, is balanced if the loops are identical and parallel so that a uniform magnetic field Bz links zero net flux into the loops.

In a presence of field gradient dBz/dz, on the other hand, a net flux is linked into the loop and generates an output from the SQUID. Typically, one of the loops is placed close to the source while the other serves as a reference to subtract away environmental noise that is uniform over the length the baseline. The typical baseline of a low-Tc gradiometer is 50-100mm long. However, to measure magnetocardiographs completely unshielded, the gradiometer is required to have a balance of about 1 part in 10^6. This is rather difficult to achieve with a first-order gradiometer. Thus, higher-order gradiometers are usually necessary.

In the case of high-Tc gradiometers, the use of wire is currently not a viable option. Therefore, two approaches have been adopted so far—electronic gradiometers and planar thin film gradiometers. The electronic gradiometer is constructed by subtracting the signals from two or more magnetometers[60,61]. Although the baseline of the electronic gradiometer be varied at well, its balance is limited by the linearity of the readout electronics and rejection of the background noise. To achieve sufficient balance levels, various kinds of mechanical balancing technology, such as cardanic suspensions[32] or superconducting plates[62], have been incorporated into the electronic systems.

However, mechanical balancing is not a practical solution because of its complexity and limited reproducibility.

The principles of most high-Tc planar thin film gradiometers are a straightforward extension of low-Tc planar gradiometers, which require multilayer processing on large substrates. These high-Tc thin film gradiometers either involve gradiometric flux transformers with two pickup loops connected to a multiturn input coil coupled to the SQUID[63,64] or employ two loops directly coupled to the SQUID fabricated on the same chip[65,66]. The disadvantage of these gradiometers is the short baseline, limited by the size of the substrate, typically 5-20mm, which is not sufficient for biomagnetic measurements in an unshielded environment.

In this chapter, I describe the novel technique developed at UC-Berkeley. The high-Tc planar gradiometer has a baseline of 48mm and an intrinsic balance in the z direction of about 1 part in a few hundred. In addition, a new version of our five channel high-Tc magnetocardiography system is introduced. Using this system, adult cardiograms are obtained both inside a magnetically shielded room and in an ambient environment.

3.1 Principles of Operation

The asymmetric planar gradiometer evolved from a design by Zimmerman[67] for a wire-wound, axial gradiometer coupled to a fractional-turn SQUID machined from

niobium; a thin-film low-Tc version was demonstrated by Matlashov *et al.*[68]. The first-derivative gradiometer, shown in Fig. 5-1, consists of a directly coupled magnetometer with a pickup loop of inductance Lm and area Am, and a superconducting flux transformer with an input coil of inductance Li and area Ai connected to a pickup loop of inductance Lp and area Ap. The input coil is inductively coupled to the magnetometer with a mutual inductance $M = \alpha (L_m L_i)^{1/2}$.

If a uniform magnetic filed is applied to the gradiometer [Fig. 5-1(a)], conservation of magnetic flux in the pickup loop of the magnetometer and in the flux transformer is given by:

$$B_0 A_m - L_m J_m - M J_t = 0 \tag{5.1}$$

and

$$B_0 (A_p + A_i) - J_t (L_p + L_i) - M J_m = 0, \tag{5.2}$$

where Jm and Jt are the screening supercurrents in the magnetometer loop and the flux transformer, respectively. To achieve the balance condition Jm = 0, the optimal value of mutual inductance is given by

$$M_{opt} = [A_m/(A_p+A_i)] (L_p+L_i) = \alpha_{opt} (L_m L_i)^{1/2}. \tag{5.3}$$

This result can be expressed as

$$\alpha_{opt} = \frac{L_p + L_i}{\sqrt{L_m L_i}} \frac{A_m}{A_p + A_i}. \tag{5.4}$$

It is clear that one must choose the area and inductance values so that $\alpha_{opt} < 1$.

We now apply a gradient field to the gradiometer. If a field δB_x is applied to one

84

(a)

(b)
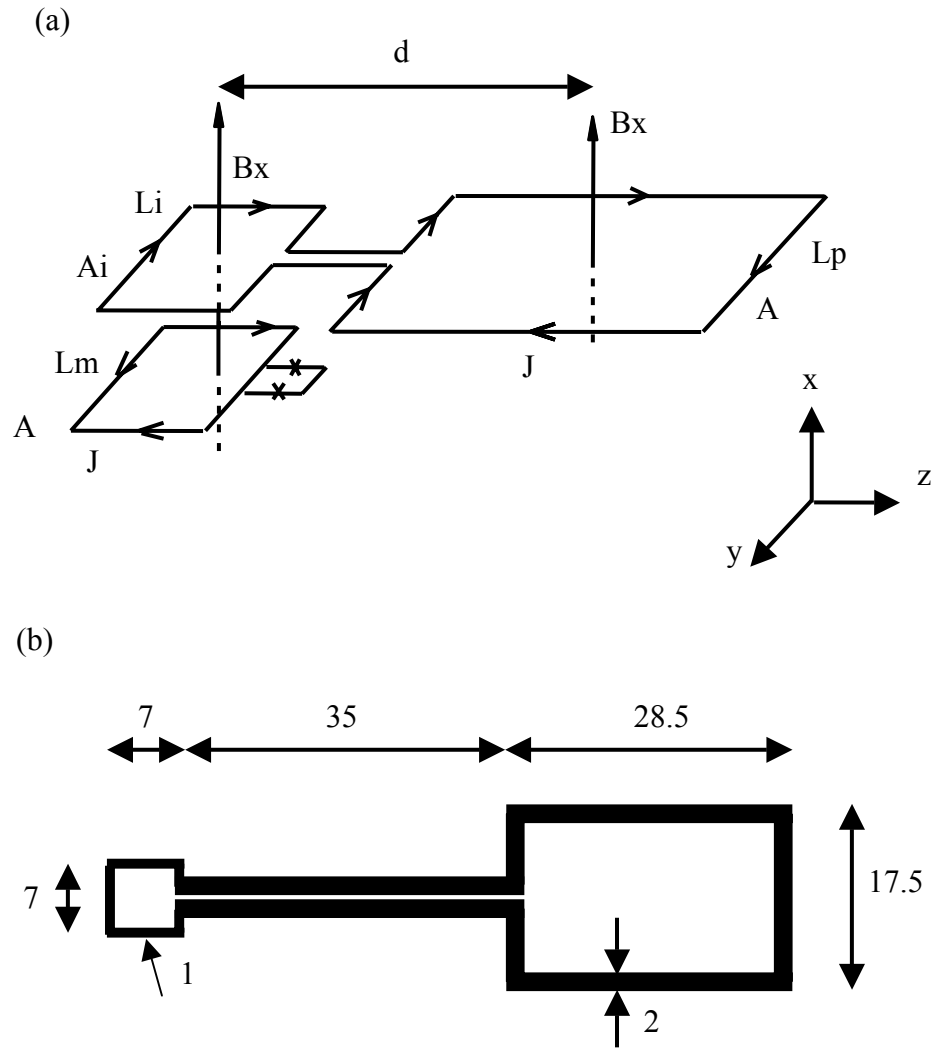
Fig. 5-1 (a) Schematic drawing of an asymmetric planar gradiometer; (b) flux transformer used in the practical device, showing dimensions in mm (not to scale).

of the loops of the flux transformer, flux conservation yields

$$\delta B x A p - (\delta J t)(L p + L i) - (\delta J m) M o p t = 0 \tag{5.5}$$

and

$$(\delta J m) L m + (\delta J t) M o p t = 0. \tag{5.6}$$

The current response of the magnetometer is

$$\delta J_m = \frac{\delta B_x A_p}{M_{opt} - (L_p + L_i) L_m / M_{opt}} = \eta \frac{\delta B_x A_m}{L_m}. \tag{5.7}$$

Here, η represents the screening effect, that is, the reduction of the sensitivity to the applied field compared to that of the bare magnetometer. With appropriate design, one can achieve $\eta \approx 1$, that is, the sensitivity of the magnetometer itself is not significantly reduced by the presence of the flux transformer.

3.2 Fabrication and Calibration

Flux transformers were fabricated from a 260nm thick YBCO film coevaporated at Conductus[69] on a 100mm diameter r-plane sapphire wafer buffered with CeO2, and patterned by photolithography and etching in a 0.05% aqueous solution of HNO3. The fabrication procedure for directly coupled magnetometers was described in chapter II. Before the two substrates were flip-chipping together, the surfaces of both the magnetometer and the flux transformer were coated with a thin layer of varnish. Using alignment marks on both substrates, we positioned the magnetometer relative to the flux transformer to an accuracy of approximately 20 μm with the aid of an optical microscope.

The two substrates were bonded together with the back side of the magnetometer against the film of the flux transformer with one or two layers of Mylar film between them. We attached them with varnish, which enables us to disassemble the device by soaking it in acetone. The complete flip-chipped gradiometer, also called a hardware gradiometer, is shown in Fig. 5-2. The outer edges of the pickup loop are patterned with grids with linewidths of 50 μm, which enable us to change the mutual inductance by removing some of the YBCO lines. All the calibrations required to choose the areas and inductances of the magnetometer and the flux transformer have been carried out by Kouznetsov et al.[70] in an extensive study.

To calibrate the gradiometer, we mount the gradiometer on a fiberglass probe with its baseline oriented vertically along the z-axis. The gradiometer is then placed at the center of a 1.14m diameter Helmholtz pair with the axis of the coils perpendicular to the plane of the device. To characterize the balance of the first-order gradiometer with respect to a field along the x-axis, in the absence of eddy currents the response of the magnetometer is given by

$$R^{(1)} = C_x^{(0)} B_x + d \frac{\partial B_z}{\partial x},$$ (5.8)

where d is the baseline and $C_x^{(0)}$ is a common mode coefficient, which defines the balance of the gradiometer in the x-direction.

A 12 Hz magnetic field is applied to the gradiometer and the output from the flux-locked SQUID is obtained. After determining the degree of imbalance, we brought the
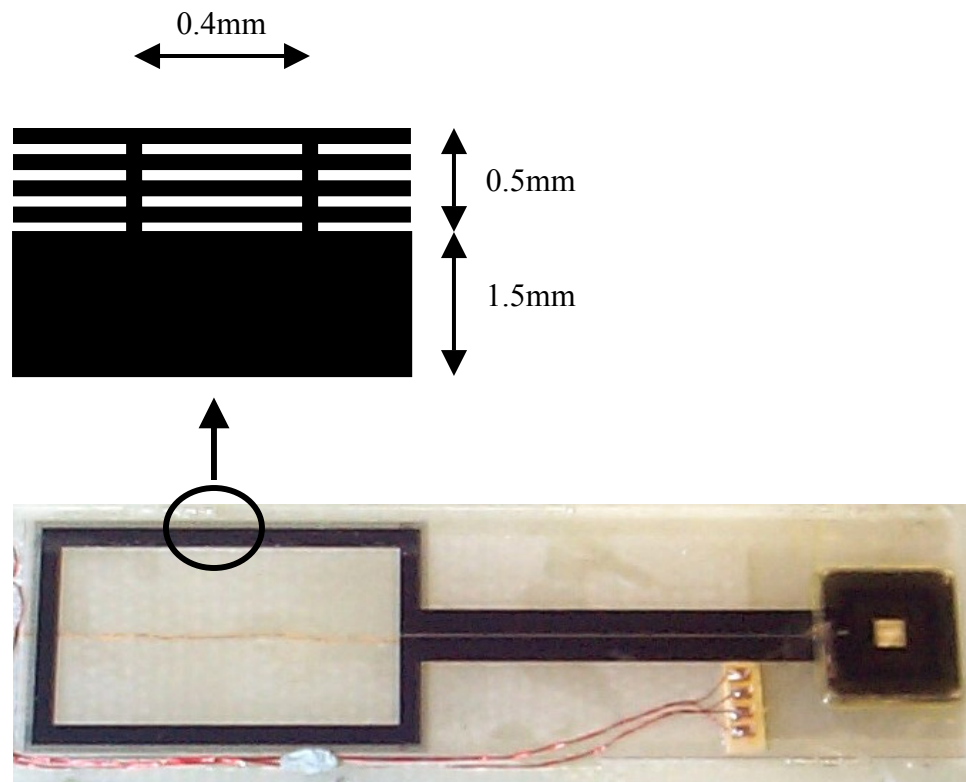
87

Fig. 5-2 Photograph of first-derivative flip-chipped gradiometer showing details of the trimming grid.

gradiometer back to room temperature and etched away a length of the YBCO line at the edge of the flux transformer. We repeat the procedure until the balance of the hardware gradiometer with respect to the out-of-plane (x direction) is 1 part in a few hundred. We also measure the balance along the y-axis by turning the gradiometer through 90° and along the z-axis by means of a second Helmholtz pair. Typically, we obtained a balance in the y- and z-directions to better than 1 part in 200.

3.3 Multichannel Magnetocardiography System

Because the component of the heart signal perpendicular to the chest is bigger than the parallel components, we constructed a new version of the five channel magnetocardiography system involving two first-derivative gradiometers and three reference SQUIDs. Figure 5-3 shows a schematic drawing of part of the system. The gradiometers are placed at the bottom of the insert against the end of the dewar with a separation of 90mm. The gradient field we are measuring now is $\partial \mathrm{Bz}/\partial \mathrm{x}$. The three reference SQUIDs are mounted on a cube; we can change the position of the cube relative to the plane of the gradiometers from 50 mm to 150mm. The reference SQUIDs are patterned into 4μm lines. All the devices were hermetically sealed inside capsules containing heaters made of manganin wire embedded in Stycast 1066.

All parts of the insert were machined out of phenolic material to eliminate metallic components. The wires are twisted in pairs and encased in Teflon tubing. Those
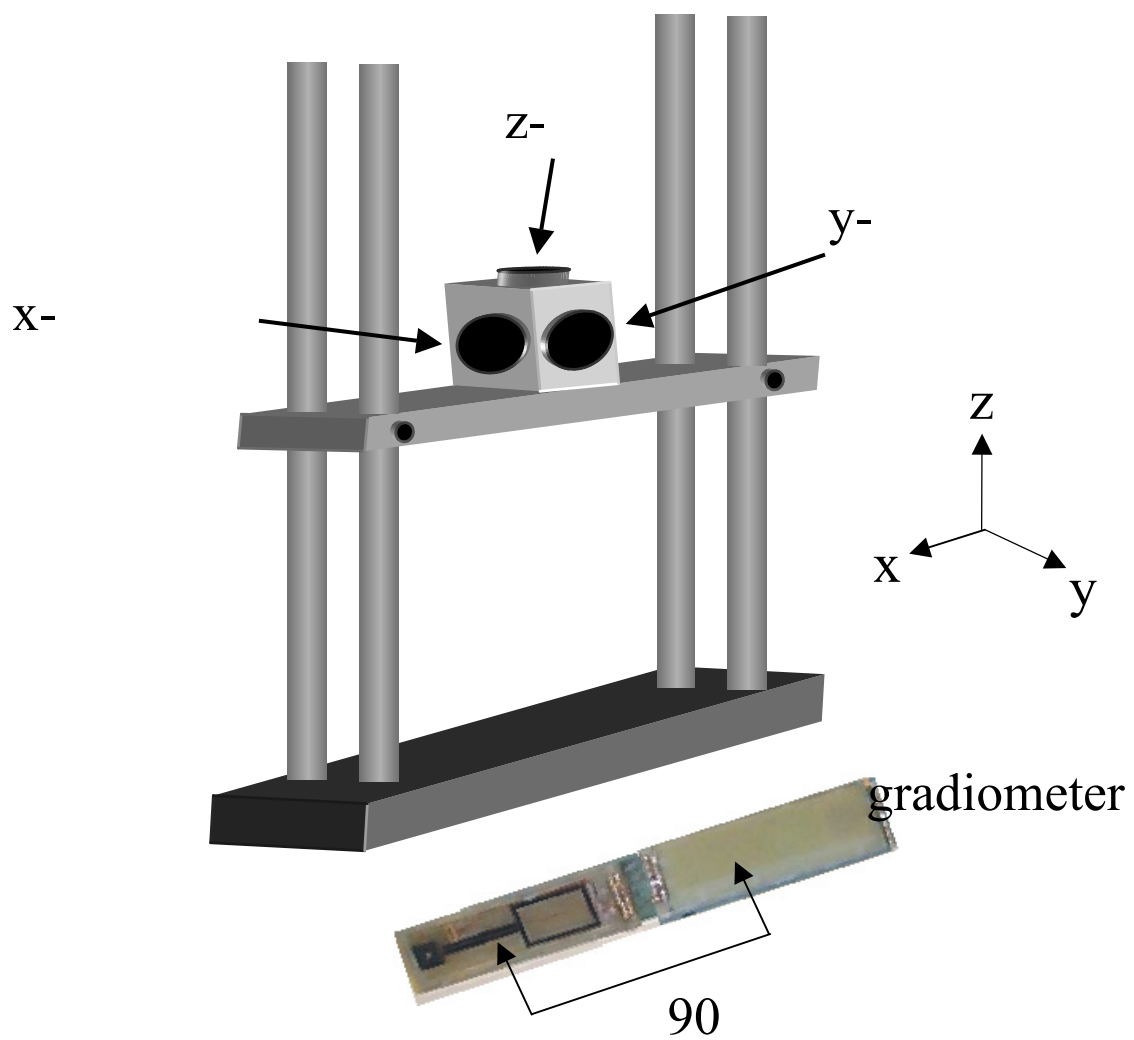
Fig. 5-3 Schematic drawing of the bottom part of the insert.

pairs connected to the output of SQUIDs are surrounded by grounded CuNi tubes. The insert and the devices are made at UC-Berkeley and the calibration and cardiogram measurements were carried out in Low Temperature Division and Biomagnetic Center at University of Twente in the Netherlands.

The measurements were carried out in a dewar 250mm in diameter covered by a layer of copper mesh[71] to exclude rf interference. For calibration, the system is placed at the center of a 1.5m square Helmholtz pair. The SQUIDs were operated using a Conductus PFL-100 flux-locked loop (see Sec. 3.3). Data acquisition and analysis were performed with Labview software[72]. During the subtraction process, the uncorrelated noise signal from the reference SQUIDs is scaled down by the reduction factor of the gradiometer, and added to the noise signal of the gradiometer. For example, for a gradiometer balanced to 1 part in 100, the noise signal of the reference SQUIDs is scaled down by 100 and then added to that of the gradiometer. The sensitivity of the directly coupled magnetometers in the white noise region is 50-70 $fT/Hz^{-1/2}$. As a result, the thermal noise of the reference SQUIDs should be less than 5 $pT/Hz^{-1/2}$. Each of our narrow-line reference magnetometers has a white noise in the range 0.6-0.9 $pT/Hz^{-1/2}$. Figure 5-4 shows the noise of the SQUIDs from the five-channel system taken in a well shielded environment.

To assess the degree to which we can improve the balance using software, we applied a 12 Hz uniform field and recorded the output signals from the SQUIDs. Using common mode correction, which subtracts signals of the hardware gradiometer from
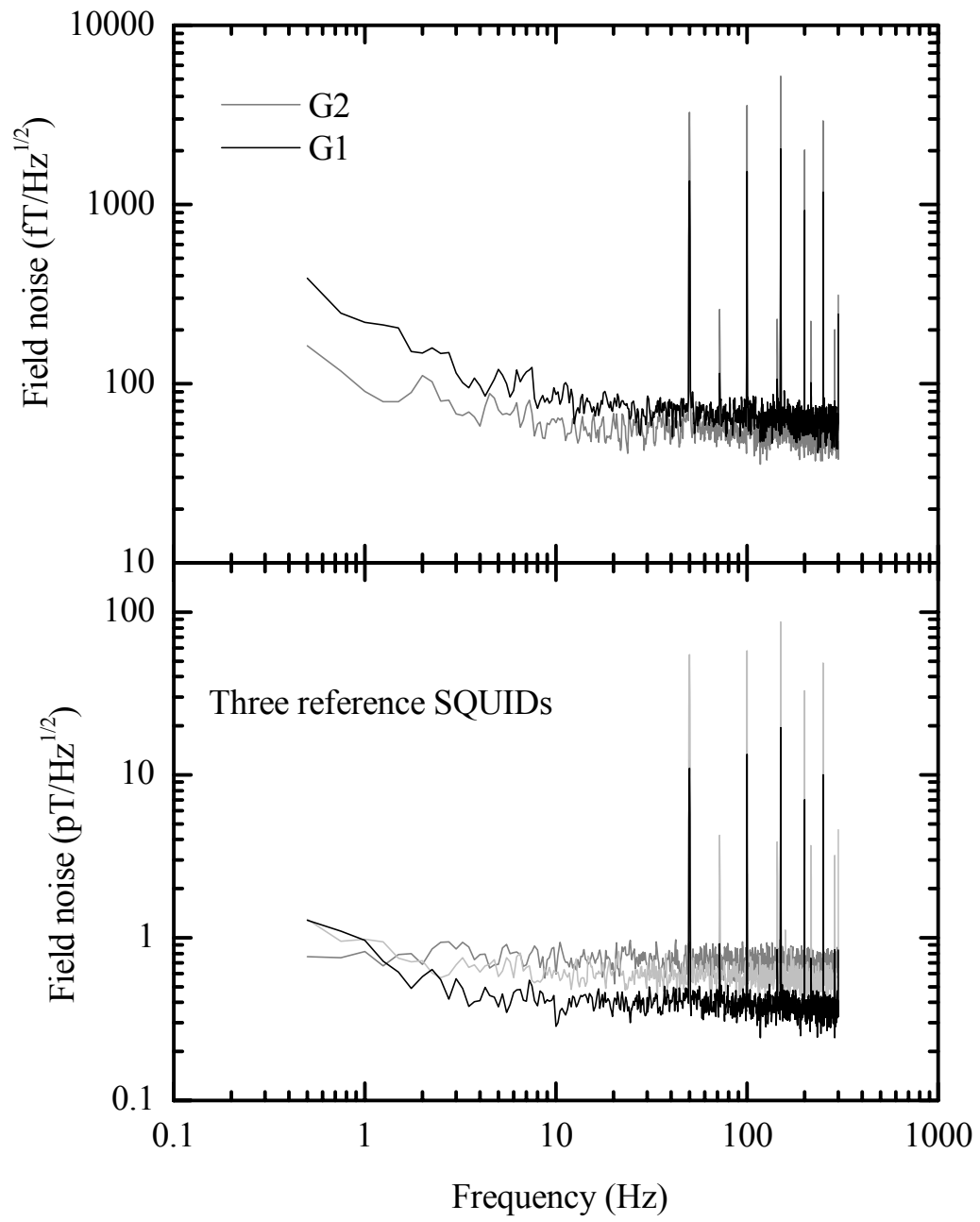
Fig. 5-4 The noise spectra of (a) two gradiometer (G1 and G2) and (b) three reference SQUIDs.

those of the reference SQUIDs, we obtained a response from the software balanced gradiometer which is at least a factor of 50 lower than that from the hardware gradiometer. In other words, with an aid of reference SQUIDs the software gradiometer can attenuate applied magnetic fields to 20-50 parts per million. The balance coefficients C_x, C_y, and C_z are chosen adaptively to fulfill a certain criterion for system performance. Adaptive balancing is used to maximize the signal–to-noise ratio.

3.4 Magnetocardiography in Ambient Fields

Measurements on cardiograms have been carried out in Biomagnetic Center in Twente in collaboration with Dr. M. ter Brake. We first recorded adult magneto-cardiograms inside the magnetically shielded room (MSR). The dewar was placed on a wooden structure. The volunteer lay on a wooden bed which can be moved in three directions. The signals from the reference SQUIDs and reference gradiometer, weighted by appropriate balancing coefficients, were added to the signal from the sensing gradiometer. Note that, because of the low interference from the power line inside the MSR, we did not apply notch filters to these data. On the other hand, we used a third-order band-pass filter to limit the bandwidth of MCG measurements to between 0.3 Hz and 50 Hz. The MCG data were recorded in real time[44]. In addition, we also have the option of saving raw data from all five channels and analyzing the data off-line to look for an improvement in the signal-to-noise ratio. Figure 5-5 shows a cardiogram taken inside MSR. In fact, it is sufficient to use one gradiometer while taking MCG inside the MSR.
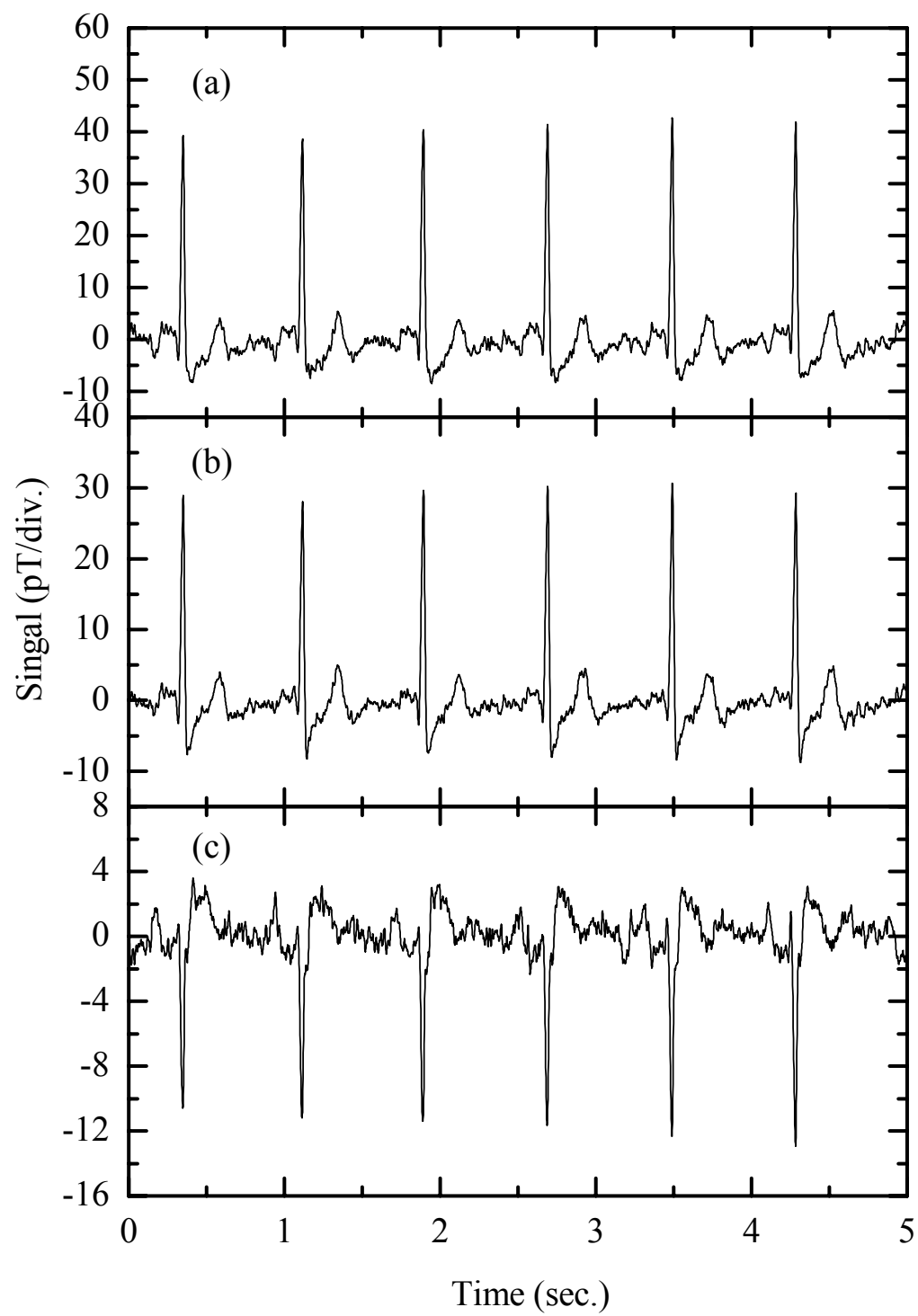
Fig. 5-5 Real-time adult magnetocardiograms taken inside the MSR; (a) signal from second-order gradiometer, (b) signal from gradiometer G1 (the sensing gradiometer) and (c) signal from gradiometer (G2).

We then moved the system about 4m away from the MSR. The volunteer now sat on a chaise lounge and the dewar was tilted about 30° toward the human subject as shown in Fig.5-6. Data processing is the same as for data taken inside the MSR. Additionally, the power line noise at frequencies 50 Hz and 100 Hz was digitally filtered by second-order power elliptic notch filters centered at these frequencies.

Figure 5-7 shows an adult MCG in an unshielded environment. As the environmental noise is now much more higher than in the MSR, the second-order gradiometer is required. Figure 5-7 compares the signals from the second-order and first-order gradiometers for the same data set. The features of the QRS peak and T-wave show clearly on the second-order gradiometer but the signals from the first-order gradiometers are barely visible. To improve the signal-to-noise ratio, one can average signals over a time interval. Figure 5-8 shows the signal from Fig. 5-7(a) averaged over 38 beats with a bandpass filter between 0.3Hz and 50 Hz. The noise is significantly reduced by this process.

We have demonstrated a successful technique combining high-T_c planar gradiometers with software balancing for measuring MCG in an unshielded environment. The cardiograms have sufficient quality for clinical applications.

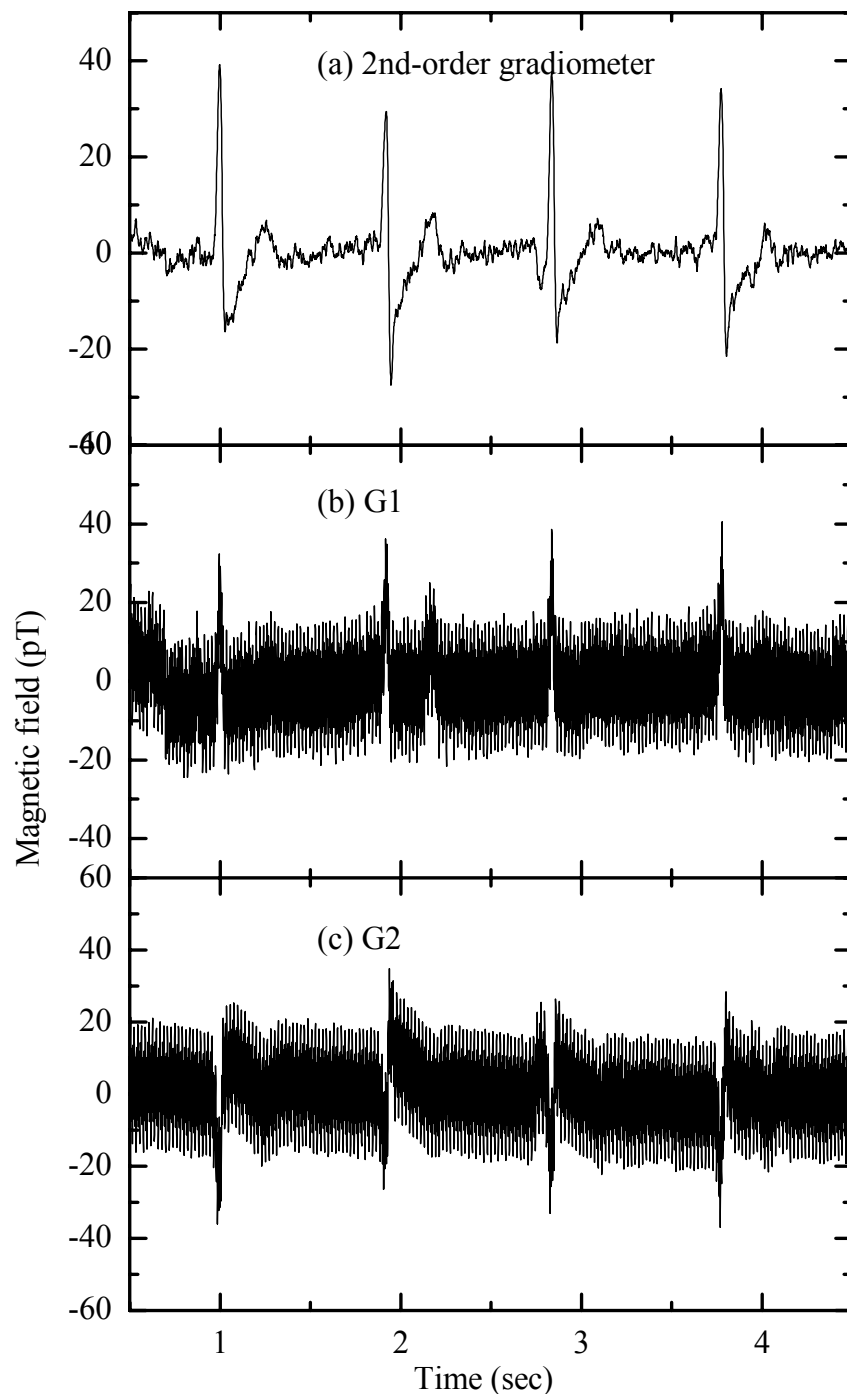Fig. 5-6. Photograph of the MCG system.

Fig. 5-7 Adult cardiograms measured in ambient environment (a) signal from second-order gradiometer, (b) signal from sensing gradiometer G1, and (c) signal from gradiometer G2.
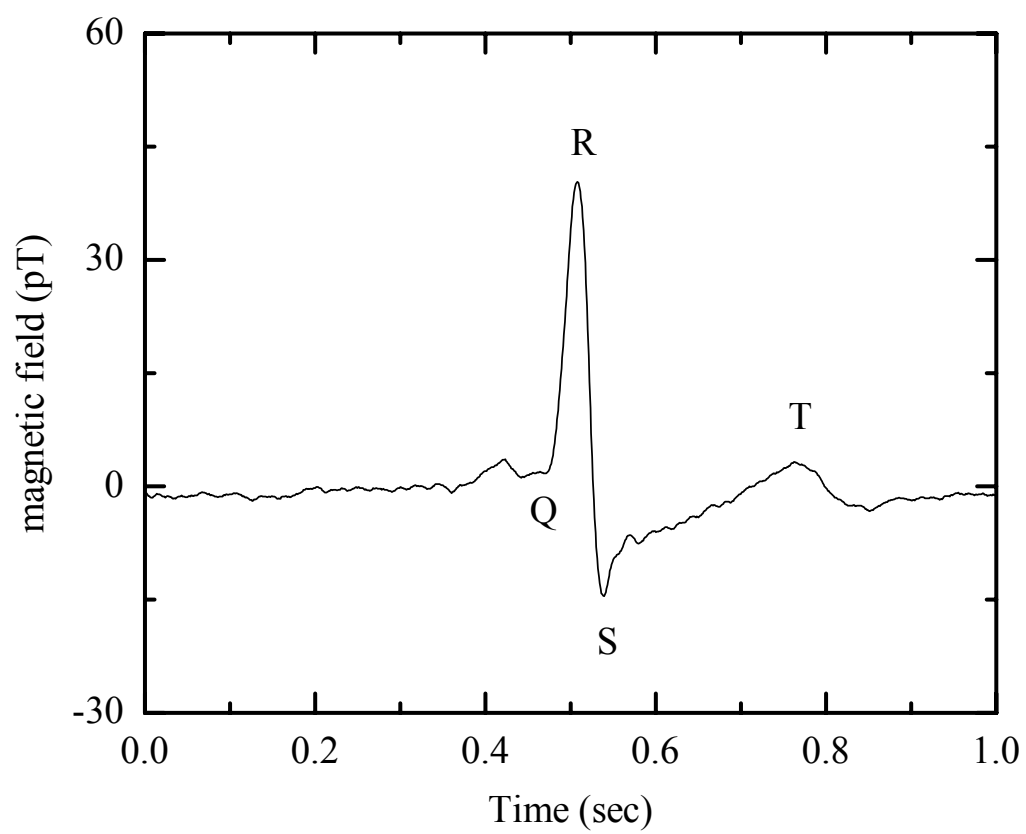
Fig. 5-8 Unshielded magnetocardiogram averaged over 38 beats.

Chapter VI

Conclusions and future directions

The goal of this work was to develop high-Tc SQUID devices that are suitable for practical applications in ambient magnetic fields. By incorporating 4 μm wide lines into SQUIDs, directly coupled magnetometers and multilayer magnetometers, we were able to eliminate the intrinsic 1/f noise due to thermally activated hopping of flux vortices in YBCO films when the devices were cooled in a static magnetic field below the threshold value, 100μT. An extra bonus from adopting narrow lines in the SQUID devices is the increase in their effective areas, which leads to moderate increases in sensitivity, typically 10%. Since this work was published, narrow lines have become the trend in designing SQUID devices for operation in ambient fields. However, it is crucial to have high quality thin films and 4 μm lines with straight cut edges.

In a second set of measurements, we cooled the SQUID devices in a magnetic field which was subsequently turned off. For a bare SQUID, the applied threshold field at which the vortices are driven into the 4 μm wide YBCO films by the induced supercurrent current is about 12 μT. Although the applied threshold field is well below the earth's field, the SQUID can rotate in the earth's field up to 40º, which is sufficiently for most applications. In the case of multilayer magnetometers, the addition of the flux transformer lowers the applied threshold field to 5 μT. However, the field sensitivity increases by a factor of 43. Regardless of whether the devices are cooled in a zero field

or a non-zero field, the threshold field depends solely on the change in applied magnetic field.

For future multilayer magnetometers, we propose that one should reverse the sense of the input coil so that the applied threshold field can be increased, while the field sensitivity is reduced by only 5%.

This design of an MCG system based on high-Tc asymmetric gradiometers is a novel technique to detect cardiograms in an unshielded environment. Combining the hardware gradiometers and reference magnetometers with software, we demonstrated an adult cardiogram taken outside the magnetically shielded room of sufficient quality for clinical applications.

Besides measuring adult cardiograms, the group at the University of Twente, The Netherlands, is interested in taking fetal MCG as well. For a fetus in the 20th week of gestation onward, there is no suitable technique other than fetal MCG to diagnose fetal arrhythmias. Electrocardiography (ECG) is usually not measurable because of the problem of volume conduction. Echocardiography usually lacks time resolution. In addition, fetal MCG does not require one to take an image, which means that a one-channel system is sufficient. To adapt our 5 channel MCG system to measure fetal MCG, a new dewar, which will reduce the distance between the liquid nitrogen and the outside, is under construction. A computer simulation of the optimum separation of the two 1st-

order gradiometers is also in progress. With help from a pediatrician, the group at Twente and we are developing a new technique to measure fetal MCG the in near future.

On the other hand, interest in adult MCG is ongoing. Recently, CardiomagImaging (CMI) has offered several low-Tc MCG systems to hospitals to demonstrate that the technique offers advantages of speed, cost and reliability over competing methods in the detection of ischemia. It will take time to collect enough data in order to demonstrate the efficacy of this technique. However, through collaborations, doctors are working to understand the MCG technique and begin to realize that MCG can be used to diagnose ischemia and classify arrhythmias. If this technique becomes broadly applicable, it is almost inevitable that it will involve high-Tc devices, such as the one I have described in this thesis. I would be happy to see MCG systems enter mainstream medicine to diagnose disease and to save lives in the near future.

Bibliography

1 B. D. Josephson "Possible new effects in superconductive tunneling" Phys. Lett. **1,** 251-253 (1962).

2 R. C. Jaklevic, J. Lambe, A. H. Silver, and J. E. Mercereau "Quantum interference effects in Josephson tunneling", Phys. Rev. Lett. **12**, 159 (1964).

3 J. Clarke, "SQUIDs: theory and practice" in H. Weinstock and R. W. Ralston (eds.), The new superconducting electronics, pp. 123-180 (1993).

4 J. G. Bednorz and K. A. Müller "Possible high-Tc Superconductivity in the Ba-La-Cu-O system" Z. Phys. B **64,** 189 (1986).

5 M. K. Wu, J. R. Ashburn, C. J. Torng, P. H. Hor, R. L. Meg, L. Gao, N. Z. Huang, Y. Q. Wang and C. W. Chu Phys. Rev. Lett. **58**, 908 (1987).

6 W. C. Stewart, "Current-voltage characteristics of Josephson junctions", Appl. Phys. Lett. **12**, 277-280 (1968).

7 D. E. McCumber, "Effect of ac impedance on dc voltage-current characteristics of Josephson junctions", J. Appl. Phys. **39**, 3113-3118 (1968).

8 John Clarke and Roger H. Koch "The impact of high-temperature superconductivity on SQUIDs" Science **242**, 217 (1988).

9 R. C. Jaklevic, J. Lambe, A. H. Silver and J. E. Mercereau "Quantum Interference Effect in Josephson tunneling" Phys. Rev. Lett. **12**, 159 (1964).

10 Kittel and Kroemer "Thermal Physics" 2nd edition, (1980).

11 K. K. Likharev, and V. K. Semenov, "Fluctuation spectrum in superconducting point junctions", JETP lett. **15**, 442 (1972).

12 Claudia D. Tesche and John Clarke " dc SQUID: noise and optimization" J. Low. Temp. Phys. **37**, 397 (1979).

13 J. J. P. Bruines, V. J. de Waal, J. E. Mooij, "Comment on DC SQUID noise and optimization by Tesche and Clarke", J. Low. Temp. Phys. **46**, 383 (1982).

14 K. Enpuku, Y. Shimomura, and T. Kisu "Effect of Thermal Noise on the Characteristics of a High-T_c Superconducting Quantum Interference Devices" J. Appl. Phys. **73**, 7929 (1993).

15 D. Koelle, R. Kleiner, F. Ludwig, E. Dantsker and John Clarke "High-Transition-Temperature Superconducting Quantum Interference Devices" Rev. Mod. Phys. **71** (3), 631-686 (1999).

16 C. T. Rogers and R. A. Buhrman, "Composition of 1/f noise in metal-insulator-metal tunneling junctions", Phys. Rev. Lett **53**, 1272 (1984).

17 M. J, Ferrari, M. Johnson, F. C. Wellstood, J. J. Kingston, T. J. Shaw, and John Clarke J. Low. Temp. Phys. **94**, 15 (1994).

18 R. H. Koch, W. J. Gallagher, B. Bumble and W. Y. Lee Appl. Phys. Lett. **54**, 951 (1989).

19 P. Chaudhari, J. Mannhart, D. Dimos, C. C. Tsuei, C. C. Chi, M. M. Oprysko, and M. Scheuermann, Phy. Rev. Lett. **60**, 1653 (1988).

20 R. Simon, J. B. Bulman, J. F. Burch, S. B. Coons, K. P. Daly, W. D. Dozier, R. Hu, A. E. Lee, J. A. Luine, C. E. Platt, and M. J. Zani IEEE Trans. Magn. **MAG-27**, pp3209 (1991).

21 M. S. DiIorio, S. Yoshizumi, K.-Y. Yang, J. Zhang, and M. Maung Appl. Phys. Lett. **58**, 2552 (1991).

22 S. Witanachchi, H. S. Kwook, X. W. Wang, and D. T. Shaw, Appl. Phys. Lett. **53**, 234 (1988).

23 Inam, M. S. Hedge, X. D. Wu, T. Venkatesan, P. England, P. F. Miceli, E. W. Chase, C. C. Chang, J. M. Tarascon, and J. B. Wachtman, Appl. Phys. Lett. **53**, 908 (1988).

24 J. Frohlingsdorf, W. Zander, and B. Stritzker, Solid State Commun. **67**, 965 (1988).

25 Roas, L. Schultz, and G. Endres, Appl. Phys. Lett. **53**, 1557 (1988).

26 G. Koren, E. Polturak, B. Fisher, D. Cohen, and G. Kimel, Appl. Phys. Lett. **53**, 2330 (1988).

27 X. D. Wu, A. Inam, T. Venkatesan, C. C. Chang, E. W. Chase, P. Barboux, J. M. Tarascon, and B. Wilkens, Appl. Phys. Lett. **52**, 754 (1988).

28 M. Hwang, L. Nazar, T. Venkatesan, and X. D. Wu, Appl. Phys. Lett. **52**, 1843 (1988).

29 B. Eom, J. Z. Sun, K. Tamamoto, A. Argana, and R. C. Rath, Appl. Phys. Lett. **55**, 595 (1989).

30 R. L. Sandstrom, W. J. Gallagher, T. R. Dinger, R. H. Koch, R. B. Laibowitz, A. W. Kleinsasser, R. J. Gambino, B. Bumble, and M. F. Chidholm, Appl. Phys. Lett. **53**, 444 (1988).

31 , R. B. Laibowitz, R. H. Koch, P. Chaudhari, and R. J. Gambino, Phys. Rev. B. **35**, 8821 (1987).

32 T. Terashima, K. Iijima, K. Yamamoto, Y. Bando, and H. Mizaki, Jpn. J. Appl. Phys. **27**, L19 (1988).

33 C. Wellstood, J. J. Kingston and John Clarke, "Thin-film multilayer interconnect technology for YBa2Cu3O7-δ," J. Appl. Phys. **75**, 683 (1994).

34 M. S. DiIorio, K-Y. Yang, and S. Yoshizumi, "Biomagnetic measurements using low-noise integrated SQUID magnetometers operating in liquid nitrogen," Appl. Phys. Lett. **67**, 1926, (1995).

35 M. S. DiIorio, K-Y. Yang, S. Yoshizumi, J. Zhang, M. Maung, and B. Power, "Practical high Tc Josephson junctions and dc SQUIDs operating above 85K," Appl. Phys. Lett., **58**, 2552, (1991).

36 R. L. Forgacs and A. F. Warnick, Rev. Sci. Instrum. **38**, 214 (1967).

37 Drung, D., in SQUID sensors: Fundamentals, Fabrication and Applications, NATO ASI series, edited by H. Weinstock, pp.63, (1996).

38 Koch, R. H., Clarke, J., Goubau, W. M., Martinis, J. M. Pegrum, C. M. and Van Harlingen, D. J. "Flicker (1/f) noise in tunnel junction dc SQUIDs" J. Low. Temp. Phys. **51**, 207,(1983).

39 T. W. Button, N. McN. Alford, F. Wellhofer, T. C. Shields, F. S. Abell, and M. Day, IEEE Trans. Magn. **27**, 1434 (1991).

40 J. R. Clem Private communication.

41 J. Z. Sun, W. J. Gallagher, and R. H. Koch, Phys. Rev. B **50**, 13664 (1994).

42 Dieter Keolle Private communication.

43 M. Matsuda, Y. Murayama, S. Kiryu, N. Kasai, S. Kashiwaya, M. Koyanagi, and T. Endo, IEEE. Trans. Magn. **MAG-27**, 3043 (1991).

44 D. Koelle, A. H. Miklich, F. Ludwig, E. dantsker, D. T. Nemeth, and J. Clarke, Appl. Phys. Lett. **63**, 2271 (1993).

45 M. J. Ferrari, J. J. Kingston, F. C. Wellstood, and J. Clarke, "Flux noise from superconducting $YBa_2Cu_3O_{7-x}$ flux transformers," Appl. Phys. Lett. **58**, 1106, (1991).

46 H.-M. Cho, R. McDermott. B.Oh, K. Kouzentsov, A. Kittel, J.H. Miller Jr. and John Clarke "Low-frequency noise in field-cooled, directly coupled magnetometer", IEEE Trans. Appl. Supercond. **9**, 3294 (1999).

47 H. Miklich, J. J. Kingston, F. C. Wellstood, J. Clarke, M. S. Colclough, K. Char, and G. Zaharchuk, Appl. Phys. Lett. **59**, 988 (1991).

48 D. Oh, R. H. koch, W. J. Gallagher, R. P. Robertazzi, and W. Eidelloth, Appl. Phys. Lett. **59**, 123 (1991).

49 R. H. Koch, J. Z. Sun, V. Fogliette, and W. J. Gallagher, Appl. Phys. Lett. **67**, 709 (1995).

50 P. Milliken, R. H. Koch, S. L. Brown, R. A. Altman, W. J. Gallagher, S. G. Haupt, and, D. K. Lathrop. J. Appl. Phys. **82**, 6301 (1997).

51 Hsiao-Mei Cho, Y. T. Andresen and John Clarke, "Low-Frequency Noise in High-Transition-Temperature Superconducting Multilayer Magnetometers in Ambient Magnetic Fields" submitted to Appl. Phys. Lett. in May 2001.

52 M. Hämäläinen, R. Hari, R.J. Ilmoniemi, I. Knuutila, and O. Lounasmaa, Rev. Mod. Phys. **68**, 413 (1993).

53 J. Vrba, in SQUID Sensors: Fundamentals, Fabrication and Application, NATO ASI series, edited by H. Weinstock, pp.117 (1996).

54 S. N. Erné, H. D. Hahlbohm, H. Scheer, and Z. Trontetelj. The Berlin magnetically shielded room in Biomagnetism, pp.79-87 (1981).

55 D. S. Barth, W. Sutherling, J. Engel Jr., and J. Beatty, "Neuromagnetic evidence of spatially distributed sources underlying epileptiform spikes in the human brain" Science **223**, 293-296 (1984).

56 L. Romani, S. J. Williamson and L. Kaufman, "Tonotopic organization of human auditory cortex" Science **216**, 1339-1340 (1982).

57 CMI commercial magnetocardiography system.

58 J. E. Zimmerman, and N. V. Frederick, "Miniature ultrasensitive superconducting magnetic gradiometer and its use in cardiography and other application" Appl. Phys. Lett. **19**, 161 (1971).

59 M. B. Ketchen, W. M. Goubau, J. Clarke and G. B. Donaldson, "Superconducting thin-film gradiometer" J. Appl. Phys. **49**, 4111 (1978).

60 Y. Tavrin, Y. Zhang, M. Mück, A. I. Braginski and C. Heiden, "YBCO thin film SQUID gradiometer for biomagnetic measurements" Appl. Phys. Lett. **62**, 1824 (1993).

61 R. H. Koch, J. R. Rosen, J. Z. Sun and W. J. Gallagber, "Three SQUID gradiometer" Appl. Phys. Lett. **63**, 403 (1993).

62 J. Borgmann, P. David, G. Ockenfuss, R. Otto, J. Schubert, W. Zander and A. I. Braginski, "Electronic high-temperature radio frequency superconducting quantum interference device gradiometer for unshielded environment" Rev. Sci. Instrum. **68**, 2730 (1997).

63 W. Eidelloth, B. Oh, R. P. Robertazzi, W. J. Gallagher, and R. H. Koch "YBa2Cu3O7-δ thin-film gradiometers: fabrication and performance" Appl. Phys. Lett. **59**, 3473 (1991).

64 M. N. Keene, S. W. Goodyear, N. G. Chew, R. G. Humphreys, J. S. Satchell, J. A. Edwards and K. Lander "Low noise YBa2Cu3O7-δ-PrBa2Cu3O7 multiturn flux transformers" Appl. Phys. Lett. **64**, 366 (1994).

65 S. Knappe, D. Drung, T. Schuring, H. Koch, M. Klinger, and J. Hinken, "A planar YBa2Cu3O7-δ gradiometer at 77K", Cryogenics **32**, 881 (1992).

66 V. Zakisarenko, F. Schimdl, H. Schneidewind, L. Dorrer, and P. Seodel, "Thin-film dc SQUID gradiometer using a single YBa2Cu3O7-δ layer", Appl. Phys. Lett. **65**, 779 (1994).

67 J. Zimmerman, "SQUID instruments and shielding for low-level magnetic measurements" J. Appl. Phys. **48**, 702 (1977).

68 N. Matlashov, V. P. Koshlelets, P. V. Kalashnikov, Y. E. Zhuravlev, V. Y. Slobodchikov, S. A. Kovtonyuk, and L. V. Flippenko, "High sensitive magnetometers and gradiometers based on DC SQUIDs with flux focuser", IEEE Trans. Magn. **MAG-27**, 2963 (1991).

69 Thanks to Z. Lu, V. Matijasevic and K. Char at Conductus.

70 K. A. Kouzentsov, J. Borgmann and John Clarke, "High-Tc superconducting asymmetric gradiometer for biomagnetic applications", Rev. Sci. Instrum. **71**, 2873 (2000).

71 Thanks to Dr. Michael Mück for supplying the copper mesh.

72 Thanks to Jörg Borgmann and Bert Rijpma for providing the labview programs.